NASA/TP–2020-220584

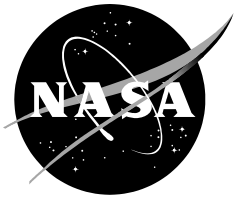

Evaluation of Fatigue Damage Accumulation Functions for Delamination Initiation and Propagation

Carlos G. Dávila, Cheryl A. Rose, Gretchen B. Murri, and Wade C. Jackson
Langley Research Center, Hampton, Virginia

William M. Johnston
Science and Technology Corporation, Hampton, Virginia

April 2020

NASA STI Program . . . in Profile

Since its founding, NASA has been dedicated to the advancement of aeronautics and space science. The NASA scientific and technical information (STI) program plays a key part in helping NASA maintain this important role.

The NASA STI program operates under the auspices of the Agency Chief Information Officer. It collects, organizes, provides for archiving, and disseminates NASA's STI. The NASA STI program provides access to the NTRS Registered and its public interface, the NASA Technical Reports Server, thus providing one of the largest collections of aeronautical and space science STI in the world. Results are published in both non-NASA channels and by NASA in the NASA STI Report Series, which includes the following report types:

- TECHNICAL PUBLICATION. Reports of completed research or a major significant phase of research that present the results of NASA Programs and include extensive data or theoretical analysis. Includes compilations of significant scientific and technical data and information deemed to be of continuing reference value. NASA counter-part of peer-reviewed formal professional papers but has less stringent limitations on manuscript length and extent of graphic presentations.

- TECHNICAL MEMORANDUM. Scientific and technical findings that are preliminary or of specialized interest, e.g., quick release reports, working papers, and bibliographies that contain minimal annotation. Does not contain extensive analysis.

- CONTRACTOR REPORT. Scientific and technical findings by NASA-sponsored contractors and grantees.

- CONFERENCE PUBLICATION. Collected papers from scientific and technical conferences, symposia, seminars, or other meetings sponsored or co-sponsored by NASA.

- SPECIAL PUBLICATION. Scientific, technical, or historical information from NASA programs, projects, and missions, often concerned with subjects having substantial public interest.

- TECHNICAL TRANSLATION. English-language translations of foreign scientific and technical material pertinent to NASA's mission.

Specialized services also include organizing and publishing research results, distributing specialized research announcements and feeds, providing information desk and personal search support, and enabling data exchange services.

For more information about the NASA STI program, see the following:

- Access the NASA STI program home page at http://www.sti.nasa.gov

- E-mail your question to help@sti.nasa.gov

- Phone the NASA STI Information Desk at 757-864-9658

- Write to:
  NASA STI Information Desk
  Mail Stop 148
  NASA Langley Research Center
  Hampton, VA 23681-2199

NASA/TP–2020-220584

Evaluation of Fatigue Damage Accumulation Functions for Delamination Initiation and Propagation

Carlos G. Dávila, Cheryl A. Rose, Gretchen B. Murri, and Wade C. Jackson
Langley Research Center, Hampton, Virginia

William M. Johnston
Science and Technology Corporation, Hampton, Virginia

National Aeronautics and
Space Administration

Langley Research Center
Hampton, Virginia 23681-2199

April 2020

Available from:

NASA STI Program/Mail Stop 148
NASA Langley Research Center
Hampton, Virginia 23681-2199
Fax: 757-864-6500

Contents

Abstract

The present report follows on the cohesive fatigue damage model methodology proposed in NASA-TP-2018-219838. In that report, an empirical function describing the incremental damage due to cyclic loading was used to calculate fatigue damage within a cohesive formulation. The form of the function was developed such that, when integrated at a constant stress amplitude from no damage to failure, it produces a life versus load response that is consistent with an S-N diagram. Therefore, the parameters of the damage model could be obtained by fitting the model predictions to an S-N diagram. The finite element analyses performed demonstrate that the cohesive fatigue accumulation function provides a link between the S-N diagram that describes crack initiation, and the Paris law that characterizes the rate of crack propagation. However, when the model was proposed, it was not known whether the form of the damage accumulation function associated with a desired S-N diagram is unique and, if not, if the link between S-N and the Paris law is unique and independent of the fatigue function selected. In the effort described herein, several alternative forms of the damage function that reproduce the desired features of S-N diagrams were found and evaluated. The effects of each of these functions on the predicted parameters of the Paris law and the propagation threshold are discussed. The results indicate that the predicted exponent m of the Paris law is indeed independent of the damage accumulation function. However, different functions predict different values for the pre-factor C of the Paris law. Therefore, the proper damage accumulation function must be selected by comparison with experiments. One of the new damage accumulation functions proposed herein was found to be particularly useful for analysis because of the ease with which the model parameters can be determined with a minimal amount of experimental information. The effectiveness of the proposed methodology and damage function was demonstrated by conducting analyses of a double cantilever beam test, a mixed-mode bending test, and a three-point bending test of a skin/doubler specimen. The results indicate that the same set of model parameters can provide accurate predictions of the rate of fatigue crack propagation for a variety of material interfaces, mode mixities, load levels, and stress ratios.

1 Introduction

In many engineering applications, fatigue life under cyclic loads is calculated using stress-life diagrams, also called S-N curves [1, 2]. These curves represent the number of cycles that a material can sustain at a given stress level before failure. The data to generate these curves is obtained by cycling smooth or notched specimens until failure. The S-N curves of many materials are simple and can be approximated by straight lines in a log-log plot, as illustrated in Fig. 1a. To account for the effect of the ratio of the minimum to the maximum stress, the slope of an S-N curve can be adjusted with empirical models such as the Goodman diagram [2]. Since these calculations essentially depend on knowledge of the stress state, predicting fatigue life with S-N diagrams does not require specialized computational tools.

On the other hand, predicting fatigue crack propagation is significantly more difficult. One difficulty is that fracture mechanics tools are required because the rate of crack propagation, defined as a crack extension, da, per incremental number of cycles, dN, is a function of the energy release rate (ERR) at maximum load, G^{max}. The rate of crack propagation in fatigue is usually described with a Paris law of the form:

$$\frac{\mathrm{d}a}{\mathrm{d}N} = C\left(G^{max}\right)^{m} \tag{1}$$

where C and m are material constants that depend on the stress ratio and mode mixity. On log-log axes, Eq. 1 is a straight line relating da/dN to G^{max}, as shown in Fig. 1b. In the remainder of this report, the term "Paris law" will refer to this line rather than to the specific form of Eq. 1. The rate of propagation described by the Paris law is capped on the low end by a threshold below which cracks do not propagate, and by quasi-static fracture on the high end.

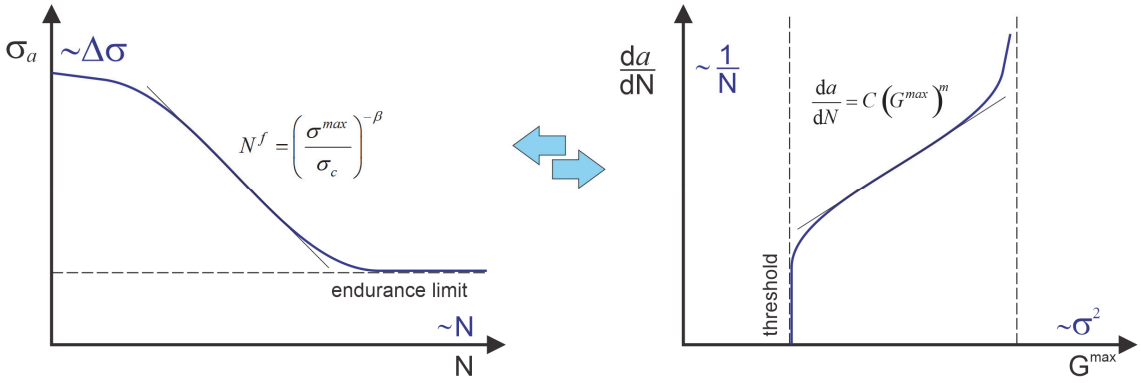

a) Stress-life diagram (S-N) b) Rate of crack propagation

Fig. 1. Relationship between the S-N curve (left) and the Paris law (right) (adapted from [3]).

In the model proposed by the first author in [4], fatigue damage inside a cohesive law envelope accumulates according to a simple two-parameter damage law at a rate that depends on the displacement jump. The two parameters of the damage law are obtained by fitting a function to the S-N diagram corresponding to the desired stress ratio. The S-N diagram can be experimental or it can be approximated with techniques used in engineering design. In the present work, an approximation of the S-N diagram that does not rely on fatigue-specific material properties is used. For additional information on the procedure, refer to references [4] and [5].

The most important question addressed in [5] is whether a cohesive model based on an S-N curve can predict the propagation rates described by the Paris law corresponding to the S-N curve. The work relied in part on the assumed relationship between S-N and crack propagation rates illustrated in Fig. 1 (adapted from Alderliesten [3]). The graph of the S-N curve in Fig. 1a indicates that the axes of the curve are proportional to the number of cycles and the stress amplitude. The graph of the Paris curve in Fig. 1b indicates that the axes are proportional to the square of the stress and the inverse of the number of cycles. If the graph of the Paris law were replotted in terms N and $\Delta\sigma$, it would look similar to the S-N curve, such that the two linear portions would correspond to each

other and the threshold portion of the propagation rate would become the endurance limit of the S-N curve. For a direct match, the replotting would also have to account for the scale effects that relate strength and fracture toughness. This relationship between the S-N and Paris laws was investigated with a semi-analytical procedure by Allegri for mode II [6], and later by Blanchfield for mixed mode [7]. Allegri and Blanchfield demonstrated that the exponents β and m of the S-N and Paris laws, respectively, are related as $\beta = 2m$. The factor 2 results from the quadratic relation between energy release rate and stress shown in Fig. 1b. More recently, Allegri [8] developed a unified formulation for fatigue onset and growth where the pre-factor C of the Paris law is obtained in terms of the length of the process zone and the exponent of the Paris law. In the following sections, these relations between the quasi-static response, the fatigue damage initiation described by S-N diagram, and the Paris law are evaluated by means of finite element implementations of a cohesive damage model for fatigue. The main objective of the present report is to investigate the effects of several alternative forms of the damage accumulation function on damage initiation and propagation.

The present paper is organized as follows. Section 2 describes the cohesive fatigue damage accumulation function proposed in 2018 [4], which is referred to here as CF18. In Section 3, the ability of CF18 to predict crack propagation rates and the possibility to calibrate the model are evaluated by examining the results of a double cantilever beam (DCB) test and a mixed-mode bending (MMB) test. Then, three new damage accumulation functions are proposed and evaluated. The first consists of an extended form of CF18 and is referred to as CF18-Ext. The second is a damage function inspired by Allegri [6], called here A12. Then, a new damage model referred to as CF20 is demonstrated. It will be shown that all of these models predict the same exponent of the Paris law but different values of the pre-factor C. Using these results, some recommendations are made regarding the accuracy of the predictions and ease of determining the parameters for each model.

2 A Cohesive Fatigue Model Based on an Assumed S-N Diagram

The S-N curve is one of the simplest descriptions of the failure of a material as a function of the applied cyclic load. The S-N curve of a brittle material does not have a low-cycle plateau, so it can be described by a single value: the value of the endurance limit [2], defined as the maximum stress that can be sustained for 10^7 cycles. In addition, the endurance limit can be estimated quite easily from the material strength. As early as the 19th century, Goodman [9] observed that the endurance limit of steels subjected to fully reversed axial loading is approximately equal to 1/3 of the yield strength. Fleck [10] performed fatigue tests on materials including polymer foams, elastomers, woods, polymers, composites, metallic alloys, and engineering ceramics and confirmed that the ratio $\sigma_e^{max} / \sigma_c = \varepsilon = 1/3$ is a good approximation for the relative endurance limit of a wide range of materials subjected to fully reversed axial loads ($R = -1$).

The endurance limit in shear is lower than for axial loads [1], so the following correction factor for the effect of fracture mode mixity, B, was proposed in [4]:

$$C_L = 1 - 0.42\,B\,. \tag{2}$$

The relative endurance limit for mixed mode and $R = -1$ is then:

$$\varepsilon_{mixed} = C_L \, \varepsilon \, . \tag{3}$$

The effect of the stress ratio, R, on the endurance limit can be estimated using the Goodman relation, which results in the following expression for the relative endurance limit as a function of mode mixity and stress ratio [5]:

$$E = \frac{\sigma_e^{max}}{\sigma_c} = \frac{2C_L \varepsilon}{C_L \varepsilon + 1 + \left(C_L \varepsilon - 1\right) R} \quad . \tag{4}$$

Equation 4 is an expression for the maximum relative stress that a material can endure for 10^7 cycles without failure. This expression for E is a function of stress ratio, R, and mode mixity, B, and will be referred to simply as the endurance, in contrast to ε, which is the relative endurance limit for fully reversed axial loading ($R = -1$ and $B = 0$).

The values of the endurance for several typical values of R calculated with $\varepsilon = 1/3$ are listed in Table 1. It can be observed, for instance, that in mode I, $E = 0.53$ for $R = 0.1$.

Table 1. Endurance as a function of stress ratio, *R,* for mode I and $\varepsilon = 1/3$.

R	***E***
-1	$\frac{1}{3}\ \left(=\varepsilon\right)$
0	$\frac{1}{2}$
0.1	0.53
0.5	$\frac{2}{3}$

2.1 Cohesive Fatigue Damage Model (CF18)

Consider the unnotched bar subjected to tensile cyclic loads shown in Fig. 2. A fatigue crack through the center of the bar is represented with a cohesive interface. The opening of the interface, or displacement jump of the cohesive law, is labeled λ. A two-piece failure of the bar occurs after N^f cycles, which depends on the maximum applied stress, σ^{max}, and the life specified by the S-N diagram.

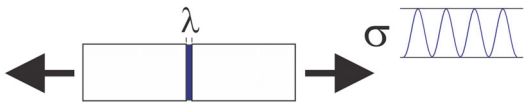

Fig. 2. Unnotched bar subjected to cyclic loads.

A bilinear cohesive fatigue law is illustrated in Fig. 3a. The outline of the cohesive law is composed of an elastic range, 0-*S*, followed by the "tearing" line, *S*-*T*. Since any point outside of

the cohesive outline corresponds to a failed material state, the outline represents the envelope of the damage process.

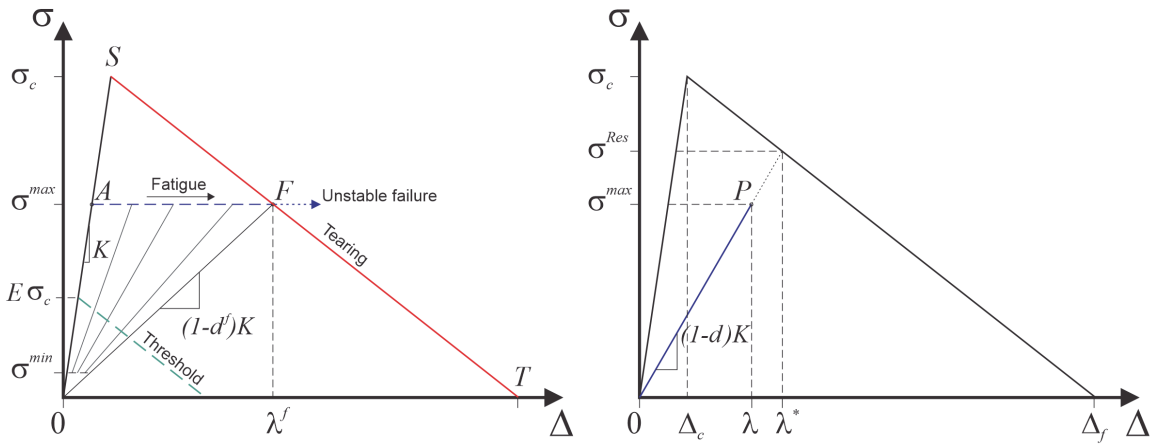

a) Description of fatigue under σ^{max} = constant. b) Definition of displacement jumps in fatigue.

Fig. 3. Cohesive law with fatigue damage – definition of failure envelope and variables.

When σ^{max} is less than the strength σ_c, the material experiences damage in fatigue without ever traversing the portion *A*-*S*-*F* of the cohesive law. Instead, at any point *P* (Fig. 3b) damage *d* accumulates with the number of cycles. Consequently, the maximum displacement jump λ increases gradually from point *A* to point *F*. At point *F*, σ^{max} exceeds the load-carrying ability of the material defined by the tearing portion *S*-*T* of the cohesive envelope and unstable failure ensues.

The evolution of fatigue damage is an unknown function of the applied cyclic load and the damage state. Heuristic power-laws of the damage increment have been proposed and justified by invoking concepts of self-similarity, where the exponent β can be seen as a stress-amplification exponent [11]. In the present work, an incremental damage function of the following form is investigated:

$$\frac{\mathrm{d}d}{\mathrm{d}N} = f\left(\lambda^{\beta}\right). \tag{5}$$

The following heuristic fatigue damage accumulation model, referred to here as CF18, was developed based on its ability to reproduce the S-N diagram and the independence of the results from the cohesive penalty stiffness. The number 18 in the name of the model refers to the year in which it was initially proposed.

$$\frac{\mathrm{d}D}{\mathrm{d}N} = \left(D+\gamma\right)\left(\frac{\lambda}{\lambda^{*}}\right)^{\beta}. \tag{6}$$

The displacement jumps λ and λ^{*} are defined in Fig. 3b, and β and γ are the two parameters of the model. The relative displacement jump at any point *P* inside the cohesive envelope is

$$\frac{\lambda}{\lambda^*} = \frac{SF}{(1-D)}. \tag{7}$$

where the stress factor is defined as $SF = \frac{\sigma^{max}}{\sigma_c}$ and the damage norm, *D,* is [12]:

$$D = \frac{\lambda^* - \Delta_c}{\Delta_f - \Delta_c} \tag{8}$$

where *D* can be interpreted as the ratio of the energy dissipated during the damage process over the critical energy release rate. Consequently, *D* is also the ratio of the damaged area over the area associated with the local discretization [12]. As Eq. 8 indicates, *D* is a linear function of λ^* and it is independent of the penalty stiffness. The loss of stiffness (1-*d*) of the cohesive law is related to *D* as follows:

$$1 - d = \frac{(1-D)\Delta_c}{D\,\Delta_f + (1-D)\Delta_c}. \tag{9}$$

The threshold of propagation occurs when the relative displacement jump is below the endurance, *E,* (Eq. 4):

$$\text{if} \quad \frac{\lambda}{\lambda^*} \le E, \ \text{then} \ \frac{dD}{dN} = 0. \tag{10}$$

For the one-dimensional constant-amplitude problem considered in Fig. 2, the total number of cycles from *A* to unstable failure (point *F* in Fig. 3a) can be calculated by integrating Eq. 6 for the range of damage $D = 0$ to D^F. The result is:

$$N^f = (SF)^{-\beta} \int_0^{D^F} \frac{(1-D)^\beta}{D+\gamma}\, \mathrm{d}D \tag{11}$$

where D^F is the damage at point *F* (Fig. 3a), which is:

$$D^F = 1 - SF. \tag{12}$$

Equation 11 represents the number of cycles to failure under a constant amplitude cyclic load in terms of the maximum stress factor SF. It has the form of the Basquin law of fatigue [13] times an integral term that is approximately constant for stress ratios below 95%. For these stress ratios, Eq. 11 satisfies Miner's cycle-ratio summation theory:

$$\sum \frac{n_i}{N_i^f} = 1 \tag{13}$$

where n_i is the number of cycles of stress σ_i applied to the specimen, and N_i^f is the life corresponding to σ_i.

The parameters β and γ that define the damage model in Eq. 6 can be obtained by fitting the life function expressed by Eq. 11 to a desired S-N curve. The next section outlines the procedure to determine the values of these parameters.

2.2 Determination of Parameters β and γ

The fitting of an S-N curve with Eq. 11 is achieved by specifying two anchor points, *(SF_1; N_1)* and *(SF_2; N_2)*. The first point corresponds to a high maximum stress ratio that represents the end of the low-cycle fatigue portion of the S-N curve. In ductile materials, the range between the first cycle and the first anchor point can be significant. In the present study, this point is arbitrarily set equal to two cycles, which translates into a short ductile range that appears to fit data [14] shown in Fig. 4. The second anchor point is set by the endurance limit corresponding to a desired stress ratio. This endurance can be obtained experimentally or calculated using Eq. 4. The anchor points that were selected are reported in Table 2.

Table 2. Anchor points used to define an S-N curve.

	$SF_i = \sigma^{max} / \sigma_c$	N_i (cycles)
Low cycle limit	0.99	2.
Endurance point	E	1×10^7

The parameters of the model are obtained by substituting the anchor points in Table 2 into Eq. 11, which results in the following system of two nonlinear equations in the two unknowns β and γ:

$$\begin{aligned} \left(0.99\right)^{-\beta} \int_0^{D_{0.99}^F} \frac{\left(1-D\right)^{\beta}}{D+\gamma}\,\mathrm{d}D - 2.0 = 0 \\ E^{-\beta} \int_0^{D_E^F} \frac{\left(1-D\right)^{\beta}}{D+\gamma}\,\mathrm{d}D - 10^7 = 0 \end{aligned} \tag{14}$$

where $D_{0.99}^F$ and D_E^F are the values of the damage parameters at unstable failure for $SF = 0.99$ and $SF = E$, respectively. These values are obtained using Eq. 12. The equations are solved numerically and tabulated for the range of stress ratios of interest. Using Fleck's assumption, $\varepsilon = 1/3$, in lieu of experimental data makes β and γ material-independent, so they do not need to be recalculated for different material interfaces.

The parameters β and γ for several typical stress ratios are reported in Table 3, and the corresponding S-N curves are shown in Fig. 4. The curve for $R = 0.1$ is solid to highlight the fact that the test data [14], also shown, corresponds to this stress ratio.

The fatigue damage model described above was implemented as a UMAT material subroutine for Abaqus [15]. The analyses are conducted using a simplified cyclic loading (SCL) procedure that avoids the computational expense of having to cycle the applied load. In SCL, the maximum load is held constant. For simplicity, the frequency of cyclic loading is 1 Hz, so that the analysis pseudo-time represents the number of cycles. The effect of cycling on fatigue damage is accounted by the stress ratio R within the constitutive damage model. The analysis is conducted in two steps.

The first step from 0 to 1 introduces the applied load (force or displacement). No fatigue damage is allowed in the first step. During the second step, the applied load is held constant but the solution is recalculated to account for the internal load redistribution that occurs with fatigue and tearing damage accumulation. The standard convergence criteria in Abaqus automatically adapt the time increments as required for an optimal convergence rate of the equilibrium iterations. One limitation of the SLC is that the stress ratio is assumed to be equal to the ratio of the applied load. In problems where there are non-proportional loads or when geometric nonlinearities induce a variation of the stress ratio throughout the structure, a technique such as Min-Max [16] is needed. The Min-Max technique consists of running two simultaneous analyses of the same model in parallel, where one model is subjected to the minimum load and the second to the maximum load. Then, the stress and damage state is communicated between the two models to calculate the local stress ratio and a common damage field.

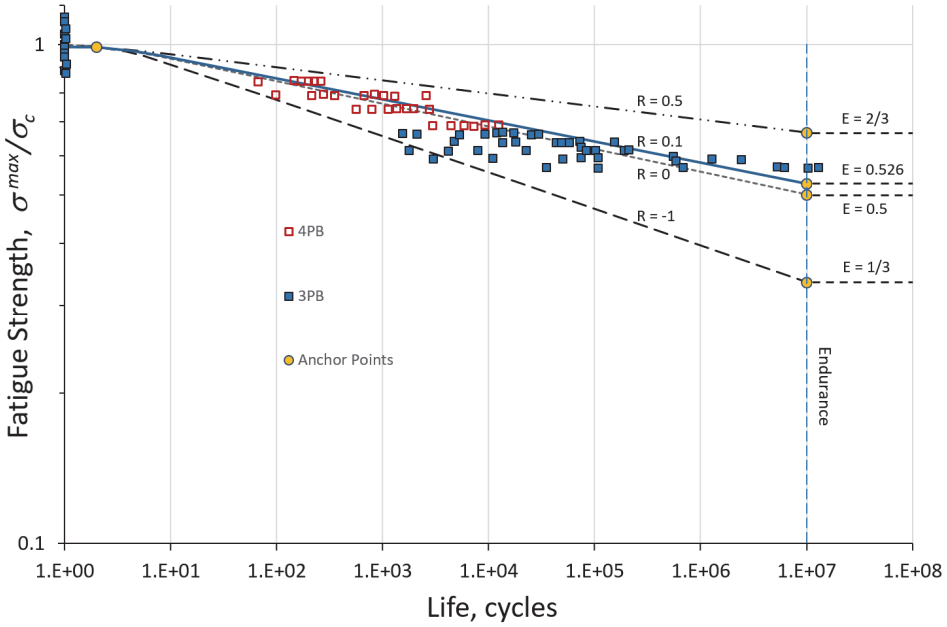

Fig. 4. S-N curves for different stress ratios obtained using Eq. 11 and the parameters shown in Table 3. The test data shown by the symbols is for $R = 0.1$ (Test data from Ref. [14]).

Table 3. Material-independent parameters (β; γ) for $\varepsilon = 1/3$ and several values of the stress ratio.

R	β	γ
-1	13.611	0.001911
0	21.842	0.002142
0.1	23.649	0.002194
0.5	38.033	0.002643

3 Evaluation of CF18 in Mode I and Mixed Mode

The analysis procedure proposed by the first author in Ref. [4] relies on three assumptions to determine the material parameters of the CF18 fatigue damage accumulation function defined by Eq. 6: (1) the quasi-static cohesive law is the envelope within which fatigue damage evolves, (2) the endurance for full load reversal ($R = -1$) is $\varepsilon = 1/3$, as observed by Fleck, and (3) the endurance E for different stress ratios can be obtained with the Goodman diagram. Using these three assumptions, delamination propagation rates were predicted without using fatigue-specific material properties or calibration. In this section, the ability of CF18 to predict the rates of fatigue propagation is evaluated in additional detail and the possibility of calibrating the model is examined. Fatigue propagation in mode I is examined in Section 3.1, and propagation in mixed mode is investigated in Section 3.2.

3.1 Analysis of Double Cantilever Beam (DCB) Test (Model CF18)

The configuration of the DCB specimen used for this study was described in Ref. [4], and the nominal dimensions are reported in Table 4. The experimental data can be found in Ref. [17].

Table 4. Dimensions of DCB specimen in mm.

a_0	b	h
50.8	25.4	2.25

The model of the DCB specimen shown in Fig. 5 was constructed in Abaqus®/Std [15]. For computational efficiency, the analyses were performed using two-dimensional (2D) plane strain models, as opposed to the three-dimensional models used for the analyses performed in previous work. The rates of propagation predicted using 2D models are about 50% higher than those predicted from 3D models due to minor differences in the compliance of the models and the effects of anticlastic curvature on the shape of the delamination front. Therefore, there are minor differences between some of the analysis results presented here and those reported previously. Since these differences are barely noticeable in a logarithmic scale, it was determined that 2D models are acceptable for the present evaluations.

Six layers of CPE4 plane strain elements were used through the thickness of each arm and cohesive elements were used between the arms to model delamination propagation. The length of the refined propagation zone in the model shown in Fig. 5 is 10 mm. The element length in this zone is 0.03 mm. A mesh convergence study indicated that an element length up to 0.1 mm is sufficiently small to predict crack length as a function of cycles, but the propagation rates can become noisy. The material properties used in the analysis, provided in Table 5, were generated within the scope of the NASA Advanced Composites Project [18].

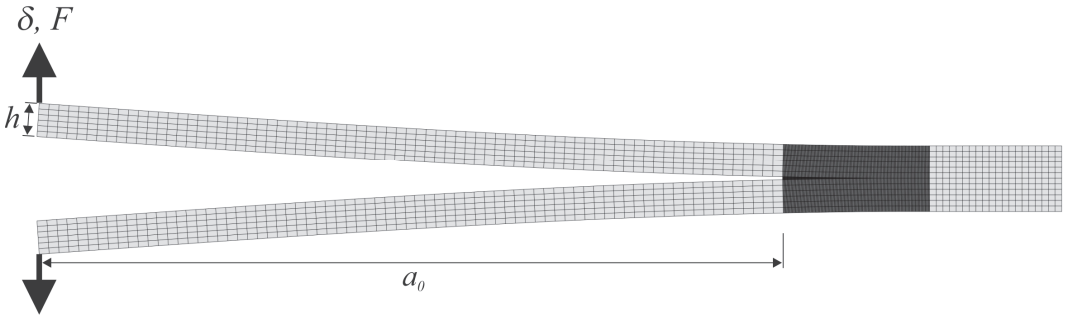

Fig. 5. Two-dimensional plane strain finite element model of the DCB specimen.

Table 5. Material properties of IM7/8552 [18].

$E_{11\ (avg\ T/C)}$	146,671.	MPa
$E_{22}=E_{33}$	8703.	MPa
$G_{12}=G_{13}$	5164.	MPa
G_{23}	3001.	MPa
G_{Ic}	0.240	N/mm
G_{IIc}	0.739	N/mm
σ_c	80.	MPa
τ_c	99.	MPa
η	2.1	
Ply thick.	0.188	mm

The values of G_c provided in Table 5 are nominal and do not account for an R-curve increase of energy release rate (ERR) with crack propagation. To account for the quasi-static R-curve response observed experimentally, two superposed cohesive elements were used that share the same nodes. The properties of one of the layers of cohesive elements represents the initiation values of fracture propagation, while the other represents the bridging properties, as described in Ref [4]. The cohesive properties for the nominal and bridge cohesive elements are summarized in Table 6.

To simulate the experimental procedure, which was conducted under displacement control, the model was loaded with a constant applied displacement, δ^{max}, and the reaction force, F, was recorded as a function of the number of cycles. The crack length, a, was calculated from the compliance $C=\delta/F$ of the model using a closed form expression derived by the corrected beam theory as discussed in Ref [4].

Table 6. Cohesive properties for nominal (unbridged) and bridged analysis.

		G_c [N/mm]	σ_c [MPa]	K [N/mm^3]
	Nominal	0.240	80.	2×10^5
superposed	Initiation	0.214	80.	2×10^5
	Bridge	0.140	0.8	2×10^3

Analyses were performed using three values of the maximum applied displacement: δ^{max} = 1.48 mm, 1.92 mm, and 2.25 mm. The results of the analyses are compared in Fig. 6 to the experimental results for four different applied loads from Ref. [17]. The blue curves represent the reference solutions obtained using the standard procedure reported in Ref. [5], i.e., the parameters of the damage model were obtained using Eqs. 4 and 14 with Fleck's assumption ε = 1/3. These blue curves are nearly identical to those reported in Ref. [5], and the minor differences between the two are due to the 2D to 3D difference discussed above, as well as the implementation of the threshold defined in Eq. 10, which was not enabled in previous work. The threshold only affects the propagation rates of the specimens subjected to the lowest applied loads.

It can be observed that the results shown in blue match relatively well the experimental values of the crack propagation rates. These three curves do not form a continuous line. Instead, the curves are shifted laterally due to the effect of the R-curve. Although the predicted results (blue) are reasonably good, the predicted propagation rates for the lowest of the three applied loads (orange data) are significantly below the experimental values, while the analyses with the higher loads overpredict the experimental results. This trend can best be observed by fitting a line through the points corresponding to a 5% increase in compliance, which corresponds to 0.9 mm of crack propagation. Comparing the blue dashed line to the corresponding (approximate) trend of the experimental results shown in a black dashed line indicates that the predicted results follow a steeper slope than the experiments.

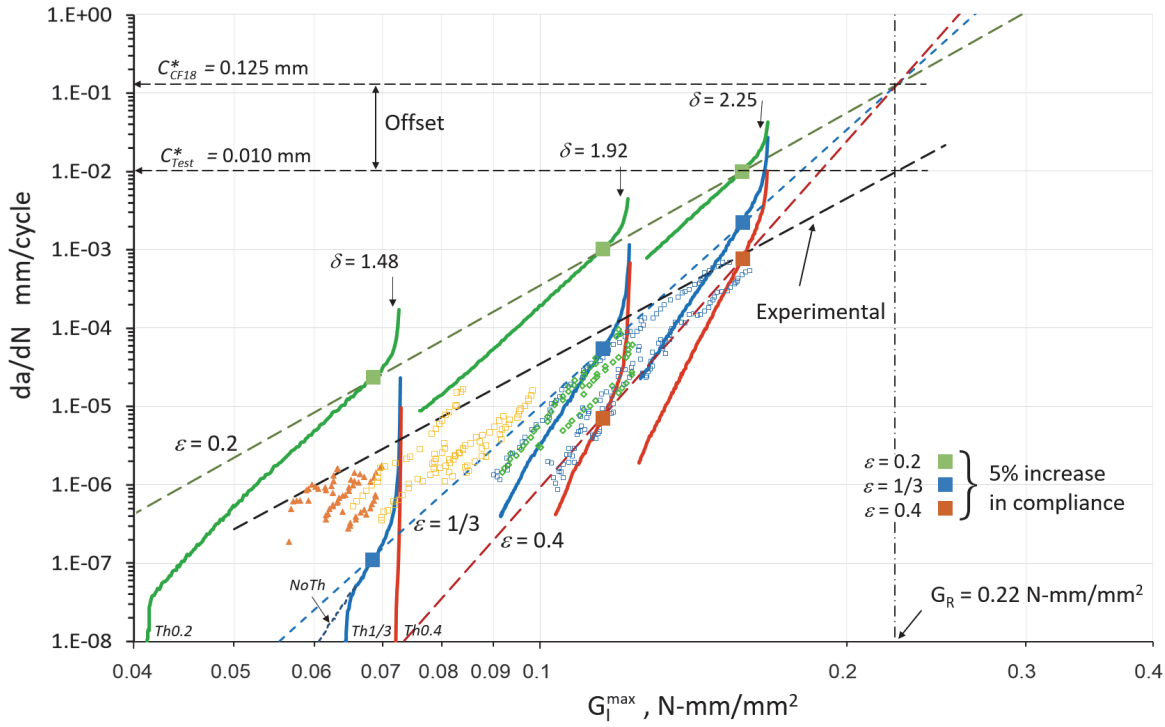

Fig. 6. Comparison of predicted delamination growth rates with experimental results (Model CF18).

One simple means to correct the slope of the analysis results is to relax the assumption on the Fleck endurance, $\varepsilon = 1/3$. In Fig. 6, additional results are shown for analyses conducted using $\varepsilon = 0.2$ (green) and $\varepsilon = 0.4$ (red). The exponents of the Paris laws through 5% compliance increases for analyses with $\varepsilon = 0.2$, 0.33, and 0.4 are m = 7.7, 11.7, and 14.6, respectively. The value of m obtained with $\varepsilon = 0.2$ is close to the experiment ($m \approx 7$), but with this endurance the analysis overpredicts the experimental rates of propagation by an order of magnitude through the entire range.

As can be expected, ε also has an effect on the threshold of propagation. The location of the predicted thresholds for the three values of the endurance are labelled *Th0.2*, *Th1/3*, and *Th0.4* in Fig. 6. For comparison, an analysis with $\varepsilon = 1/3$ was also conducted with the threshold disabled, and the corresponding curve is labelled *NoTh*.

The dashed lines for all three values of ε intersect at a pivot point on a vertical axis $G^{max} = 0.22$ N/mm^2, which is consistent with the response predicted by Allegri [19]. This value of G^{max} corresponds to the ERR of the quasi-static R-curve at a crack growth increment of $\Delta a = 0.9$ mm. If the curves in Fig. 6 were replotted in terms of $da/dN = C^* (G^{max}/G_R)^m$, they would all have the same pre-factor $C^* = 0.124$ mm, as shown in the graph. The experimental value is $C^* = 0.010$ mm. Since these values differ by an order of magnitude, the slope of the Paris line predicted with CF18 for mode I cannot be adjusted by changing ε.

3.2 Analysis of the Mixed Mode Bending (MMB) Test

The mixed-mode bending (MMB) specimens analyzed here were made with IM7/8552 tape, and they were nominally identical to the DCB specimens described in Section 3.1, including the specimen width, b, and sublaminate thickness, h. The experimental procedure is reported in [20]. The dimensions of the specimen are listed in Table 7. A finite element model of the test configuration is shown in Fig. 7. Each arm of the model is composed of four layers of CPE4 plane strain elements. In the propagation zone of the model, the mesh size in the propagation direction is 0.15 mm. This mesh is coarser than the one used for the DCB because the process zone in mixed mode is larger than in mode I. The loading lever was modeled using a multi-point constraint equation that enforces the relative vertical motion of the three points of contact. A loading arm of length c = 41.28 mm corresponds to a mode mixity of 50% [21].

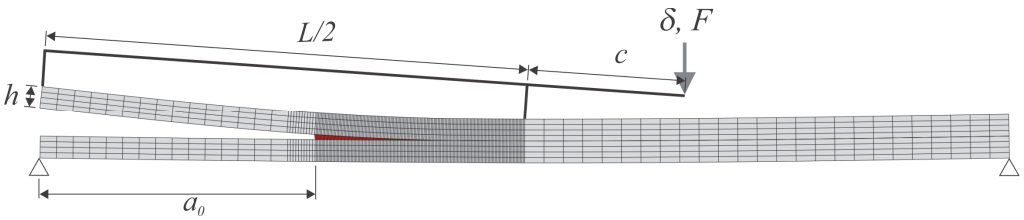

Fig. 7. Two-dimensional model of MMB specimen.

Table 7. Dimensions of MMB specimen in mm.

a_0	b	h	L	c
28.83	25.4	2.25	101.6	41.28

The material properties applied to the model are those previously reported in Table 4. No bridging was applied because the R-curve in mixed mode is less pronounced than in mode I, and because the bridging properties for mode II were not available. The analyses were conducted under force control, which is consistent with force control loading during the characterization test [20].

The results of three analyses with an applied force of F^{max} = 193 N, R = 0.1, are shown in Fig. 8 along with corresponding test data. The green, blue, and red solid lines correspond to analyses performed with endurance values of ε = 0.2, 1/3, and 0.4, respectively. The test data are represented by the symbols. At the beginning of the analysis, G^{max}/G_c = 0.32. As the crack length increases, so does the relative ERR. The process zone length during steady-state propagation, which is the band of partially damaged cohesive elements, is 1.1 mm.

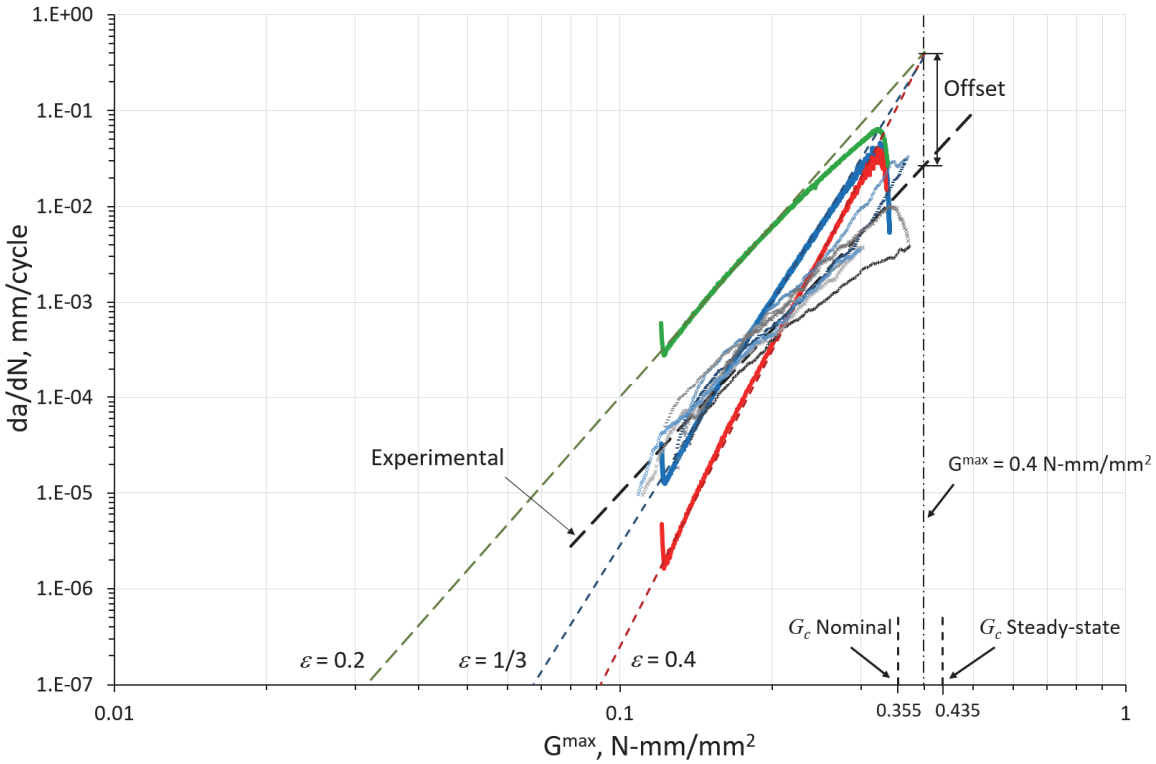

Fig. 8. Delamination growth rates in 50% mixed mode for F^{max} = 193 N, R = 0.1, and three values of ε (Model CF18).

It can also be observed in Fig. 8 that the propagation rates at the end of the simulations decrease. This decrease occurs when the crack approaches the center of the specimen, where the support of the lever arm presses down on the upper arm of the specimen and the loading condition changes.

The blue line, which corresponds to the standard endurance of $\varepsilon = 1/3$, appears to match the experimental rates of propagation well at the middle of the propagation range. However, the predicted slope of the line is higher than the experimental value. Decreasing the endurance to $\varepsilon = 0.2$ improves the predicted slope of the Paris line but, as in the case of mode I, there is an offset between the pivot point of the predictions and a line fit through the experimental data. Once again, these results indicate that CF18 cannot be adjusted by changing ε.

4 Evaluation of Alternative Damage Accumulation Functions

The preceding evaluations of the predicted rates of propagation in mode I and mixed mode indicate that the fatigue damage accumulation model defined by Eq. 6 and referred to as CF18 predicts an exponent m of the Paris law and a constant C that are too high compared to the experimental data. Therefore, it is pertinent to question the validity of model CF18 and to look for other forms of the function. It was found within the scope of this investigations that valid idealized S-N diagrams can be generated with a number of different fatigue damage functions. Therefore, it is necessary to investigate the effect of these alternative functions on the predicted values of the parameters m and C of the Paris law.

Three different forms of the damage accumulation function shown in Table 8 were developed and compared within the scope of this work. The first model, referred to as CF18-Ext is an extension of CF18 in which an additional adjustment parameter was added. The second form, A12, is inspired by a damage function proposed by Allegri [6]. Like CF18, the A12 model also uses two parameters, which are β and p. Finally, a new function referred to as CF20 that combines the advantages of the preceding forms was evaluated. The effect of the different forms of the damage function on the predicted rates of propagation is discussed in the remainder of this section.

4.1 CF18-Ext Model and Results

The cohesive fatigue damage accumulation function CF18-Ext shown in Table 8 consists of a minor extension of CF18 in which an adjustment parameter, χ, was added. When $\chi = 1$, model CF18-Ext is identical to CF18. The purpose of this modification is to investigate the effect of the adjustment factor on the predicted crack propagation rates.

The S-N function obtained by integrating CF18-Ext is

$$N^T = SF^{-\beta} \int_0^{DF} \frac{(1-D)^{\beta}}{(D+\gamma)^{\chi}} dD + 1 \,. \tag{15}$$

Table 8. Summary of three fatigue damage accumulation functions investigated.

Model	Accumulation function and S-N curve	Model parameters
CF18-Ext	$\frac{dD}{dN} = \left(D+\gamma\right)^{\chi}\left(\frac{\lambda}{\lambda^*}\right)^{\beta}$ $N^T = SF^{-\beta}\int_0^{DF}\frac{\left(1-D\right)^{\beta}}{\left(D+\gamma\right)^{\chi}}dD + 1$	$\beta, \gamma, \varepsilon$ Solve numerically for β, γ: $\left(SF_1\right)^{-\beta}\int_0^{D_{0.99}^F}\frac{\left(1-D\right)^{\beta}}{\left(D+\gamma\right)^{\chi}}\mathrm{d}D - N_1 = 0$ $E^{-\beta}\left(\varepsilon\right)\int_0^{D_E^F}\frac{\left(1-D\right)^{\beta}}{\left(D+\gamma\right)^{\chi}}\mathrm{d}D - 10^7 = 0$
A12 [6]	$\frac{dD}{dN} = \frac{\left(1-D\right)^{-p}}{p+1}\left(SF\right)^{\beta} = \frac{\left(1-D\right)^{\beta-p}}{p+1}\left(\frac{\lambda}{\lambda^*}\right)^{\beta}$ $N^T = SF^{-\beta}\left(1-SF^{p+1}\right)+1$	$\varepsilon;\quad p;\quad \beta = \frac{-7}{\log E\left(\varepsilon\right)}$ Recommended: $\varepsilon = 0.2;\ p = \beta - 1$
CF20	$\frac{dD}{dN} = \frac{1}{\gamma}\frac{\left(1-D\right)^{\beta-p}}{E^{\beta}\left(p+1\right)}\left(\frac{\lambda}{\lambda^*}\right)^{\beta}$ $N^T = \gamma E^{\beta} SF^{-\beta}\left(1-SF^{p+1}\right)+1$	$\varepsilon;\quad p;\quad \beta = \frac{-7\eta}{\log E\left(\varepsilon\right)};\quad \gamma = 10^7;\quad \eta$ Recommended: $\varepsilon = 0.2;\quad p = \beta;\quad \eta = 0.95$

It should be noted that the term "+1" at the end of Eq. 15 was added for consistency. Without the term, the number of cycles to failure for $SF = 1$ would be zero fatigue cycles. Since there is always one quasi-static cycle before fatigue starts, one cycle is added to the expression of the S-N. In previous work [4, 5], as well as in Eqs. 11 and 14, this minor inconsistency was not taken into account.

As with CF18, the model parameters β and γ are calculated by solving numerically the system of equations shown in Table 8, where $(SF_1; N_1)$ represents the left anchor point of the desired S-N curve. CF18-Ext was applied to the DCB model discussed in the previous section. Five cases were investigated, with $R = 0.1$:

- CF18: is the reference case previously shown in Fig. 6, i.e., it corresponds to an analysis using the CF18 model, including the Fleck assumption, $\varepsilon = 1/3$.
- CF18-B: uses CF18 and $\varepsilon = 0.2$ to reduce the predicted slope of the propagation rate. This case was also discussed in Section 3.1.
- CF18-Ext2-A: this model is identical to CF18-B, except that $\chi = 2$.
- CF18-Ext2-B: this model is the same as CF18-Ext-A, except that the anchor points were changed to obtain a better fit of the original S-N curve of case CF18-B.
- CF18-Ext4-C: this model is identical to CF18-Ext2-B, except that $\chi = 4$.

The details of these five models are summarized in Table 9

Table 9. Summary of model parameters for model CF18-Ext (mode I with $R = 0.1$).

Case	Stress ratio R	ε @ $R = -1$	E (Eq. 4)	SF_1	N_1	χ	β	γ
CF18	0.1	1/3	0.53	.99	2	1	23.65	0.00219
CF18-B	0.1	0.2	0.36	.99	2	1	14.56	0.00194
CF18-Ext2-A	0.1	0.2	0.36	.99	2	2	13.93	0.0685
CF18-Ext2-B	0.1	0.2	0.36	.80	80	2	14.55	0.1030
CF18-Ext4	0.1	0.2	0.36	.80	80	4	14.55	0.3334

The S-N diagrams for the five cases are shown in Fig. 9 for $R = 0.1$. Case CF18, shown in blue, has an endurance of $E = 0.53$. The remaining four cases are nearly indistinguishable because they share the same endurance, $E = 0.36$. The only case that can be identified from this group of four is CF18-Ext2-A, which bulges more at the higher stress range than the other three cases. The last two cases use a lower anchor point that results in S-N curves that are nearly identical to CF18-B.

The predicted crack propagation rates for the DCB specimen for a maximum applied displacement of $\delta^{\max} = 1.92$ mm are shown in Fig. 10. It can be observed that all of the cases with $\varepsilon = 0.2$ predict approximately the same propagation rates. It appears that the rates of propagation depend on the S-N curve and are not dependent on χ. The slopes of the predicted curves match the test results better than the reference case, but the rates are about an order of magnitude higher than the experimental results. As with CF18, attempting to adjust the predicted slope of the Paris law by changing ε from 1/3 to 0.2 in the CF18-Ext function results in propagation rates that are about an order of magnitude above the experimental results.

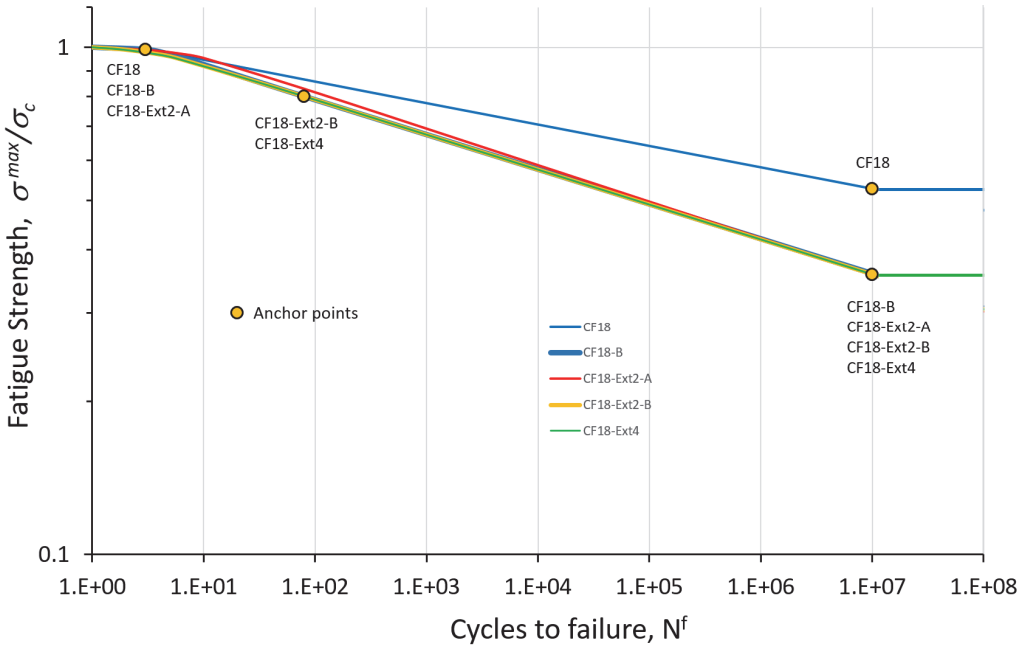

Fig. 9. S-N diagrams for mode I and $R = 0.1$ (Model CF18-Ext).

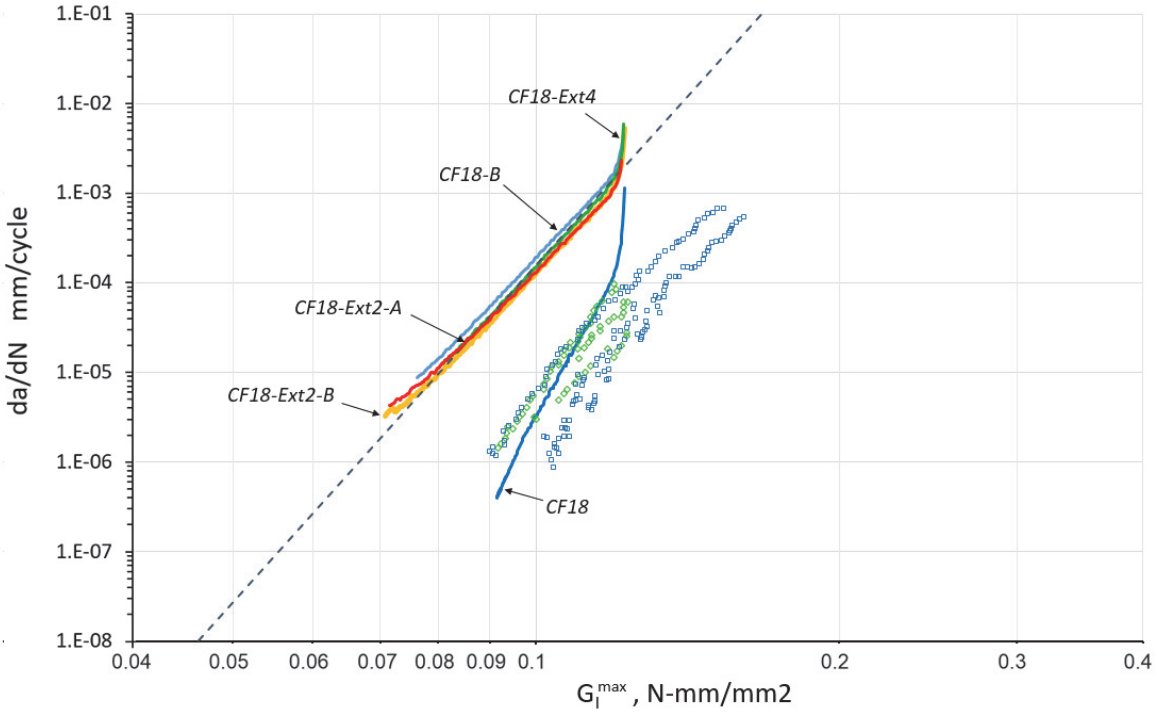

Fig. 10. Paris law for DCB specimen with $R = 0.1$ (Model CF18-Ext).

4.2 A12 Model and Results

The next damage accumulation function is an adaptation of the fatigue damage accumulation law initially proposed by Allegri [6] for propagation in mode II:

$$\frac{dD}{dN} = \frac{(1-D)^{-p}}{p+1}(SF)^{\beta}. \tag{16}$$

Equation 16 can be re-written in terms of the relative displacement jump by substituting the stress factor with the displacement jump using Eq. 7. The result is the following damage function, which we refer to as A12. (The number refers to the year of Allegri's publication.)

$$\frac{dD}{dN} = \frac{(1-D)^{\beta-p}}{p+1}\left(\frac{\lambda}{\lambda^*}\right)^{\beta}. \tag{17}$$

The S-N diagram for model A12 is obtained as described in Section 2 by integrating Eq. 16. The result is the following S-N function:

$$N^T = SF^{-\beta}\left(1-SF^{p+1}\right)+1. \tag{18}$$

The exponent β of model A12 can be calculated by observing that $SF < 1$, so that for sufficiently large values of p the term in parenthesis in Eq. 18 tends to one. Therefore, the exponent that ensures an endurance E at 10^7 cycles is

$$\beta = \frac{-7}{\log E} \,. \tag{19}$$

The S-N diagrams for two values of p (and with $\varepsilon = 0.2$) that bound all of the cases considered here are shown in Fig. 11. As it can be observed, there is no discernible difference between these two results. The S-N diagrams for these two cases are straight in a log-log plot, regardless of the value of p. The function A12 does not provide a means to simulate the "bulge" of low-cycle fatigue. Moreover, the parameter p cannot be determined, as it was for CF18, by fitting Eq. 18 to an S-N curve. However, the following results demonstrate that p does have an effect on the propagation rates.

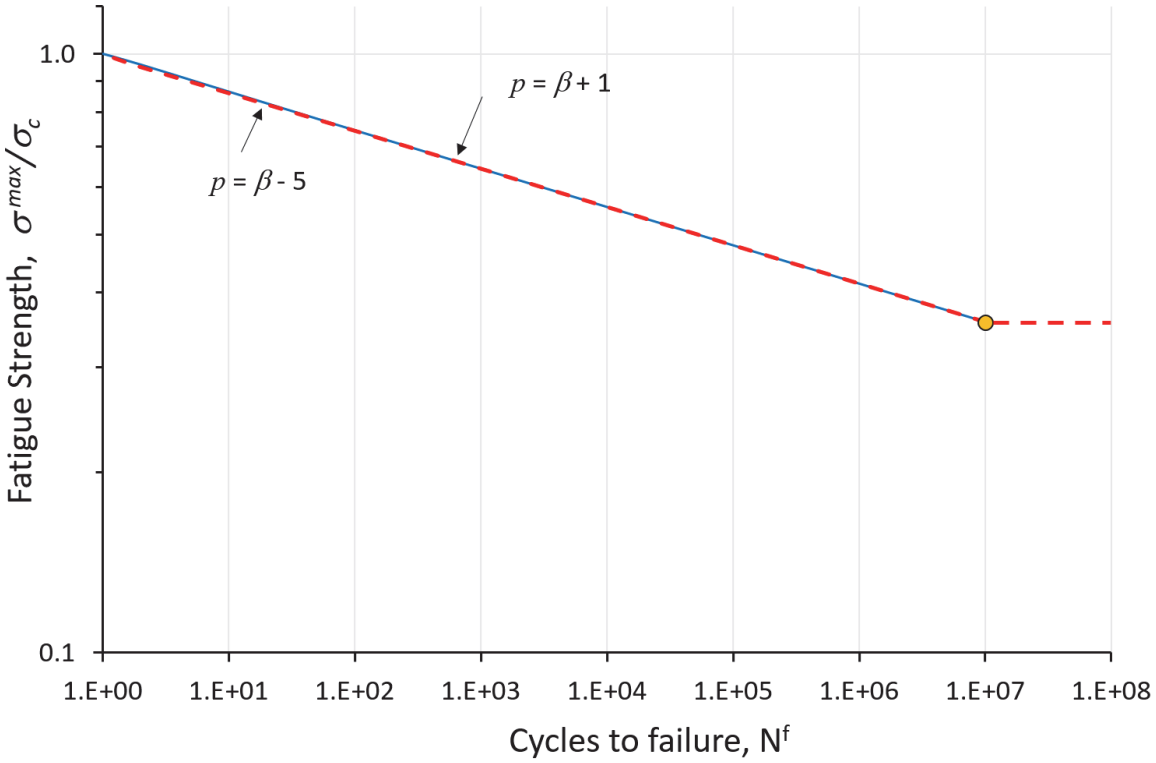

Fig. 11. S-N diagrams for mode I and $R = 0.1$ (Model A12 with $\varepsilon = 0.2$).

The results of crack propagation analyses of the DCB specimen with A12 are shown in Fig. 12 for several values of p, ranging from $p = \beta - 5$ to $p = \beta + 1$. The slopes of all of the predicted propagation curves using $\varepsilon = 0.2$ are equal, and independent of p. In addition, the predicted exponent of the Paris law drawn for $p = \beta - 1$ through the points of 5% compliance increase has a slope of $m = 7.7$, which correlates well with the experimental results ($m \approx 7$).

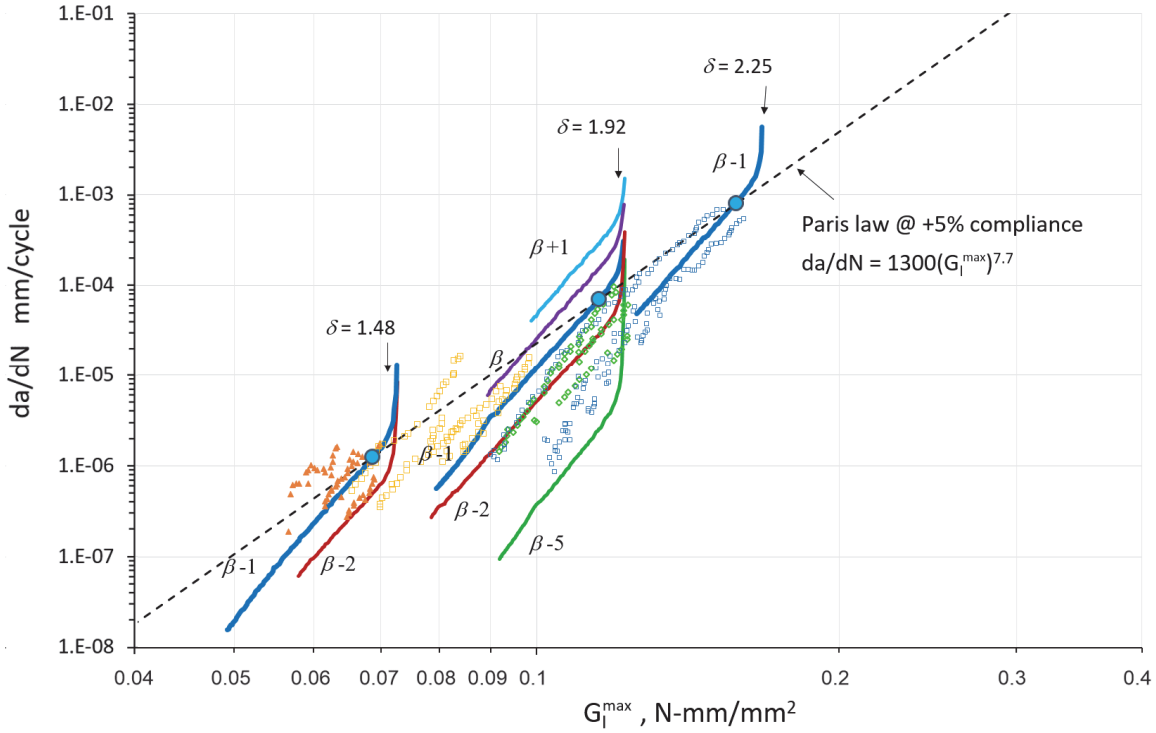

Fig. 12. Delamination propagation rates and Paris law in mode I with $R = 0.1$ (Model A12 with $\varepsilon = 0.2$).

An interesting observation of the results of the A12 function is that the predicted coefficient C of the Paris law is a function of p. Increasing p by one approximately doubles the rate of crack propagation. The results that appear to correlate best with the experimental results correspond to $p = \beta - 1$, which leads to the following simplified form of Eq. 17:

$$\frac{dD}{dN} = \frac{1-D}{\beta}\left(\frac{\lambda}{\lambda^*}\right)^{\beta} . \tag{20}$$

One important advantage of the A12 function, and the simplified form in Eq. 20 in particular, is the ease with which the model parameters are determined compared to CF18. With CF18, determining β and γ requires solving numerically the system Eqs. 14. Since that solution is computationally expensive, the results must be tabulated and interpolation used for intermediate values of R and mode mixity. With A12, β can be calculated on the fly. For instance, for the preceding case for mode I with $\varepsilon = 0.2$ and $R = 0.1$, Eq. 4 gives $E = 0.357$. Then, $\beta = -7/\log(0.357) = 15.7$. The exponent of the Paris law obtained by finite element analysis using this β is $m = 7.7$, which correlates well with Allegri's [6] semi-analytical relation between m and β, which states that $m = \beta/2 = 7.8$.

Equation 20 was also applied to the analysis of the MMB test. The predicted and experimental results for applied forces of $F^{max} = 170$, 193, and 222 N, $R = 0.1$, are shown in Fig. 13. It can be observed that the predicted results correlate well with the experimental values for the entire range of G^{max}.

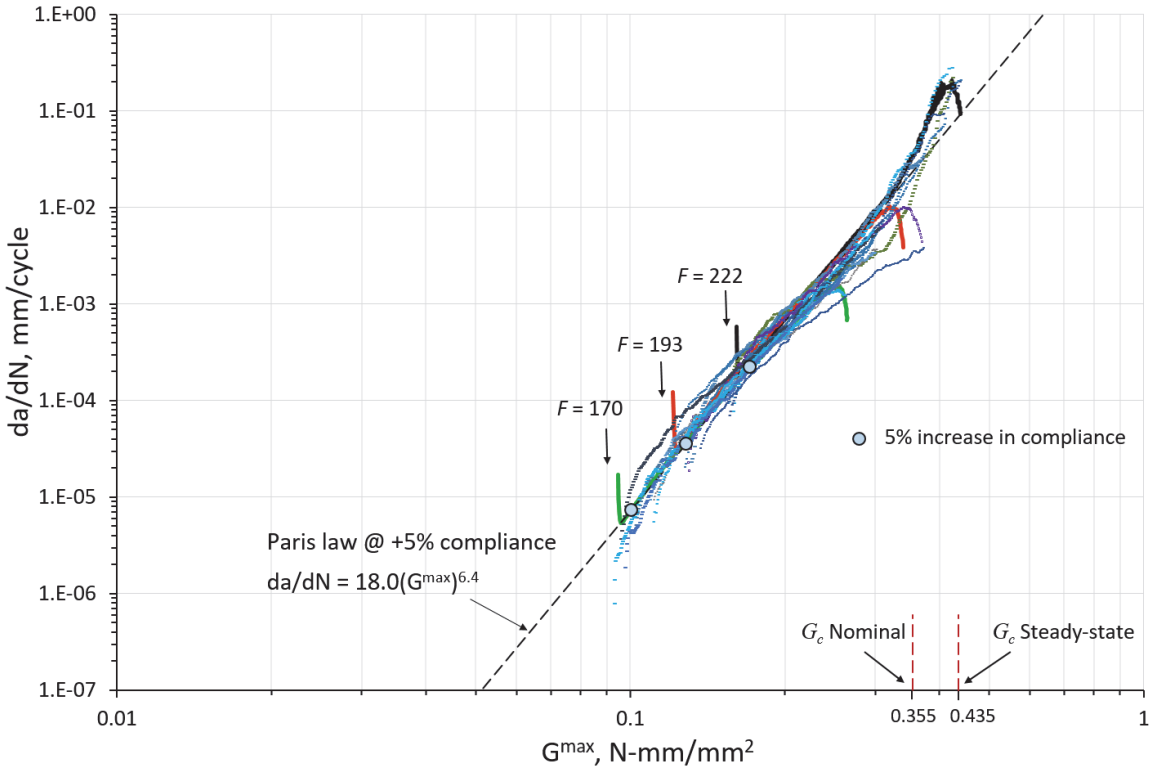

Fig. 13. Delamination growth rates in 50% mixed mode for three applied forces and $R = 0.1$ (Eq. 20 with $\varepsilon = 0.2$).

4.3 CF20 Model and Results

One drawback of function A12 is that it cannot be adjusted to account for the low-cycle "bulge" exhibited by some materials. The function CF20 was developed to provide a simple means to adjust the low-cycle range and thus mitigate this drawback of A12. CF20 has the form:

$$\frac{dD}{dN} = \frac{1}{\gamma}\frac{(1-D)^{\beta-p}}{E^{\beta}(p+1)}\left(\frac{\lambda}{\lambda^*}\right)^{\beta} \tag{21}$$

where γ is the number of cycles to endurance, which in the present work is always defined as $\gamma = 10^7$. Equation 21 can be integrated as described earlier to obtain the following S-N curve:

$$N^T = \gamma E^{\beta} SF^{-\beta}\left(1 - SF^{p+1}\right) + 1\,. \tag{22}$$

By definition, the stress ratio at endurance is $SF = E$, so the second and third terms of the RHS cancel out. The term in parenthesis tends to one, so Eq. 22 ensures that the number of cycles $N^T(E) = \gamma$ for any positive value of p. The slope of the S-N curve described by Eq. 22 is specified as:

$$\beta = \frac{-7\eta}{\log E} \tag{23}$$

where η is a "brittleness" parameter that has the effect shown in Fig. 14. When $\eta = 1$, the S-N curve is a straight line identical to that of A12. As η decreases, the S-N curve progressively develops the low-cycle "bulge" of more ductile materials. The value of p does not affect the S-N curves.

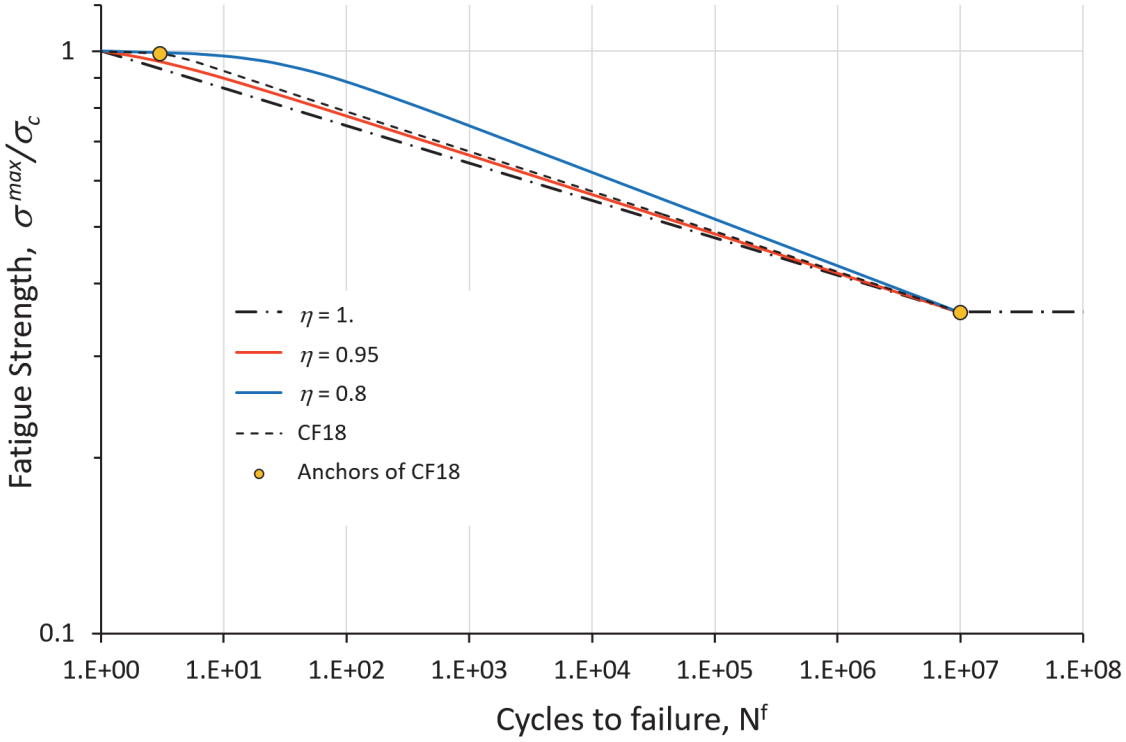

Fig. 14. S-N diagrams for mode I and $R = 0.1$ (Model CF20 with $\varepsilon = 0.2$).

The results of crack propagation analyses of the DCB specimen with CF20 are shown in Fig. 15. The analyses were conducted with $p = \beta$, $\varepsilon = 0.2$ and $\eta = 0.95$. The predicted exponent of the Paris law through the points of 5% compliance increase is $m = 7.4$, which correlates well with the experimental results ($m \approx 7$). The results with other values of p are not reported here, but the effect of p is the same as described above for function A12.

Analyses of the MMB test were also conducted, using CF20 and with $p = \beta$, $\varepsilon = 0.2$ and $\eta = 0.95$. The results for applied forces of $F^{max} = 170$, 193, and 222 N are shown in Fig. 16. As in previous analyses, the rate of propagation is initially high, and then quickly settles to a rate of propagation corresponding to the Paris law. When the crack is within 2 mm of the load application point at the center of the specimen, the rates of propagation decrease. This decrease was captured at the end of a few experimental tests. The simulation for the highest load ($F^{max} = 225$ N) does not exhibit a reduction in the rate of propagation because G_c was reached before the crack tip reached the zone under the loading node. The analysis stopped when it failed to achieve convergence of the equilibrium solution. The correlation with the experimental results is excellent.

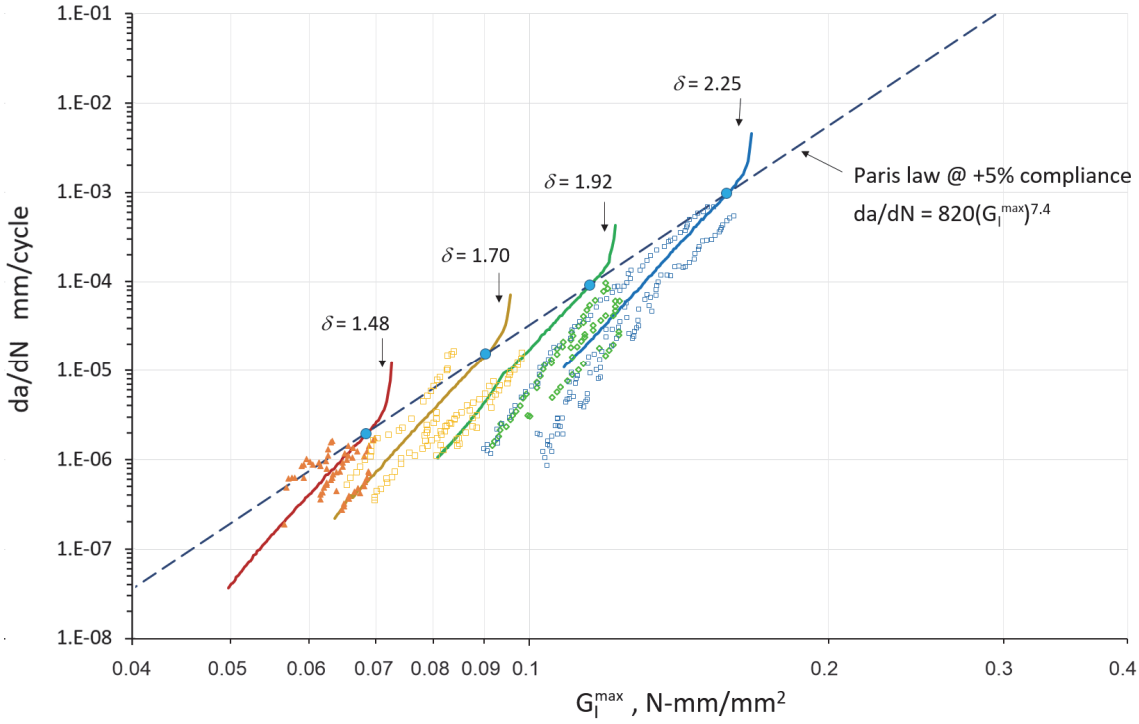

Fig. 15. Delamination propagation rates and Paris law in mode I with $R = 0.1$ (Model CF20 with $\eta = 0.95$, $\varepsilon = 0.2$, $p = \beta$).

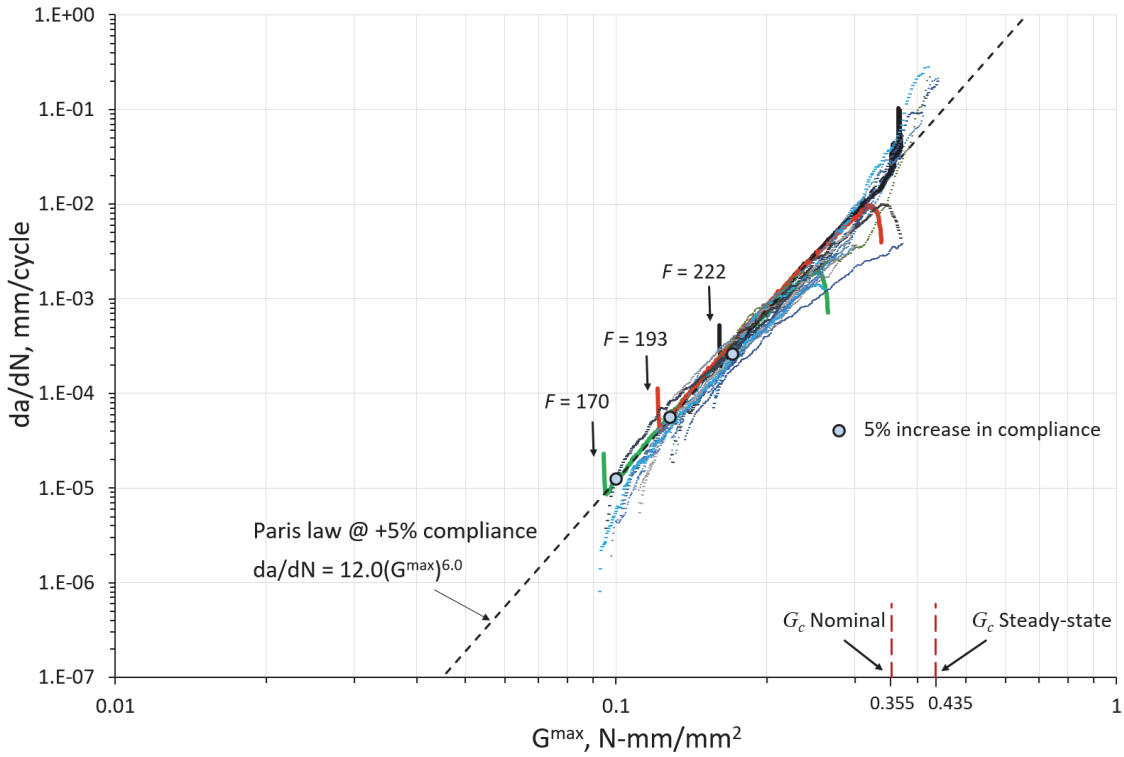

Fig. 16. Delamination growth rates in 50% mixed mode for three applied forces and $R = 0.1$ (Model CF20 with $\eta = 0.95$, $\varepsilon = 0.2$, $p = \beta$).

5 Analysis of a Three-point Bend Doubler Test

The three-point bend (3PB) doubler test described below is one of the simplest specimen configurations where deformations, local stress gradients near the flange termination, and damage processes are representative of those that develop near the flange termination of a post-buckled stiffened structure. The fatigue analysis of the skin/doubler separation in the 3PB test poses two major challenges. First, the analysis must be capable of predicting the initiation of damage from a pristine structure, which is not possible with linear elastic fracture mechanics methods and the Paris law. Secondly, the separation between the skin and the doubler for the specimen tested is not strictly a delamination: it is composed of networks of transverse matrix cracks, delaminations at several interfaces, and delamination migration paths across the plies. As a result of this damage, the effective fracture toughness of the interface increases with crack propagation to about four times the fracture toughness for initiation [22]. Predicting such complex networks of cracks requires detailed three-dimensional models and the ability to insert cracks at discrete locations. Within the NASA ACP project [18], several teams have demonstrated the ability to model these networks using either a deformation gradient decomposition damage model [23] or extended finite elements [24-26]. Similar approaches pursued for predicting fatigue damage in the same detailed manner have shown promising results [25]. However, modeling the details of the damage networks still pose some unresolved challenges.

A simpler method to analyze skin/doubler separation consists of using effective interface properties to account for the effects of the kinematic complexity of the damage on the crack growth resistance [22]. The technique used to model the effective resistance is identical to the modeling of fiber bridging used in Section 3.1, and it consists of superposing two bilinear cohesive laws, where the first law represents the initiation of fracture propagation, and the second represents the R-curve increase in the energy release rate. The cohesive fatigue model discussed above is ideally suited for predicting fatigue initiation and delamination in problems where fatigue data is not available. In this Section, we examine whether the parameters for the damage accumulation function determined in Section 4 are capable of predicting the initiation and propagation of skin/doubler separation.

5.1 3PB Test Description

The 3PB doubler test is a simple experiment designed to observe and characterize the separation failure between skin and stiffener flange. The 3PB specimens consist of 305 mm by 25.5 mm rectangular strips of skin with a co-cured 101.6 mm-long doubler at the center of the span. The doubler consists of a patch of fabric plies that represents the flange of a stiffener. The stacking sequence of the skin is $[-45/45/0/90/-45/45]_s$ unidirectional tape plies, and that of the doubler is *[-45/0/45/-45/-45/45/0/-45/-45/0/45/-45]* fabric plies. The 3PB doubler specimen is supported on two rollers with a 203.2-mm span, as shown in Figure 17.

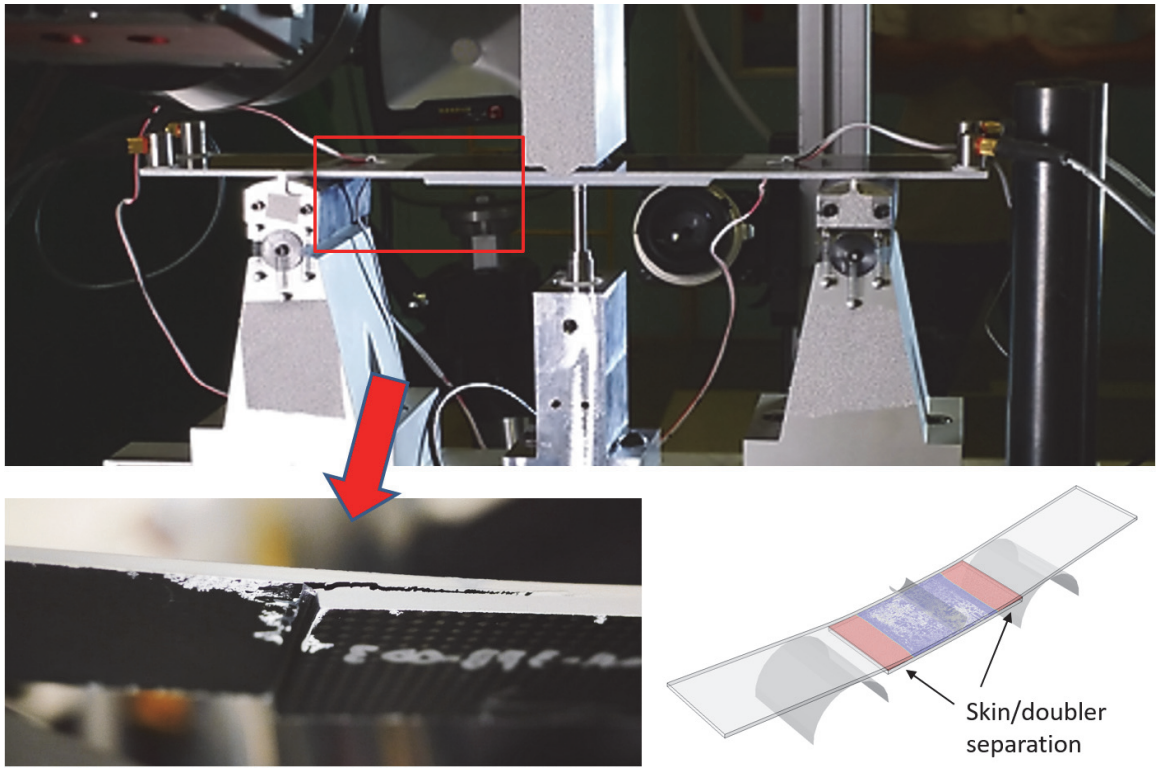

Fig. 17. 3PB doubler test and detail showing skin/doubler separation.

The 3PB specimen was tested under quasi-static and fatigue loading conditions. For both quasi-static and fatigue loading, damage in the experiments was observed to initiate in the region of the doubler termination, shown in the detail of Figure 17, as a combination of transverse matrix cracks in the outer ply of the skin (adjacent to the doubler) and delamination at the interface between skin and flange, and between the first two plies in the skin. As the load magnitude or number of cycles increased, damage propagated from each flange edge toward the doubler center, and into the skin thickness through a complex network of interacting matrix cracks and delaminations. An X-Ray computed tomography (CT) cross-section with representative damage is shown in Figure 18.

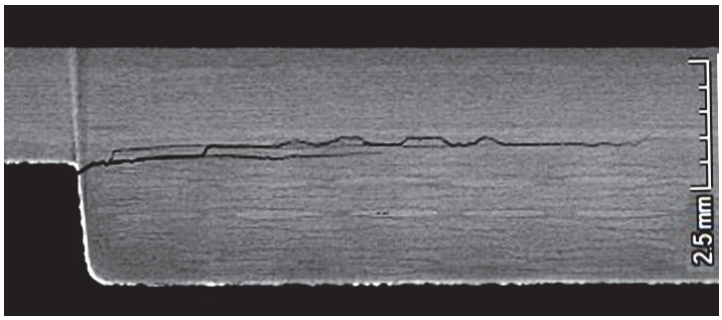

Fig. 18. X-Ray CT cross-section of flange termination area showing morphology of delamination separation.

5.2 Quasi-static Analysis of 3PB Doubler Test

Effective interface properties required for simulation of the fatigue response of the 3PB specimens were obtained by fitting the predicted quasi-static response to the experimentally observed response. The model of the 3PB doubler specimen is shown in Fig. 19. For computational efficiency, the model is symmetric at the mid-span. The width of the specimen is 25.4 mm. For computational efficiency, the model consists of 1/8 of the specimen width. The applied forces shown in the results were scaled accordingly. The load is applied through a rigid hemispherical cylinder with contact along the bottom surface of the skin. The skin is modeled with three layers of SC8R continuum shell elements, and the doubler is modeled with two layers of SC8R elements. Composite properties were applied to the elements, such that every layer of elements in the skin represents a sublaminate of four unidirectional plies, and each layer of elements in the doubler represents a sublaminate of six fabric plies. Fourteen elements were used across the width of the specimen, and the axial length of the SCR8 elements and the cohesive elements between the flange and skin laminates is 0.056 mm.

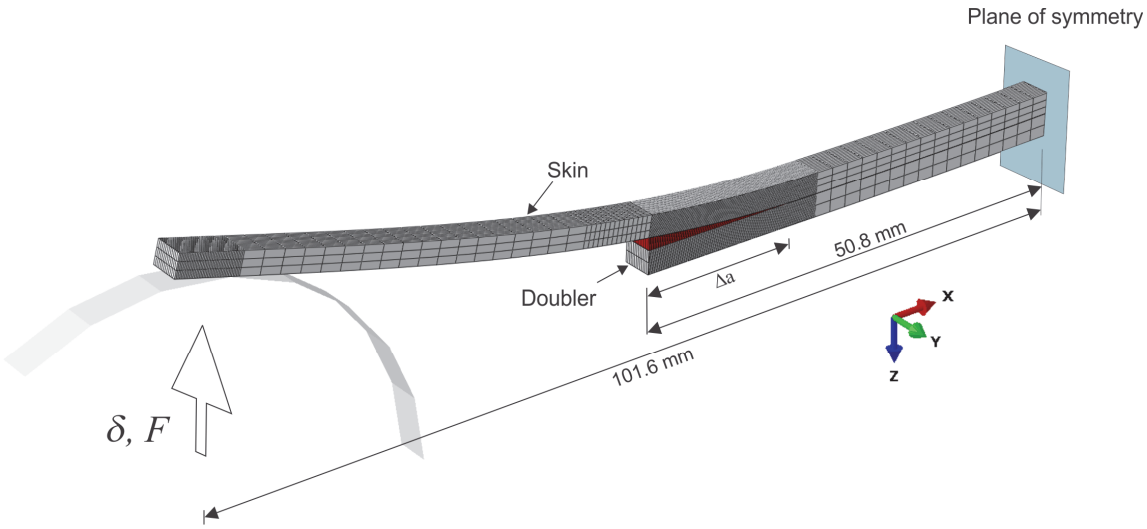

Fig. 19. Symmetric three-dimensional model of 3PB doubler test.

The elastic properties of the tape plies are identical to those of the DCB and MMB specimens and reported in Table 4. The elastic properties of the fabric plies are shown in Table 10. Ideally, the interfacial properties would be measured by performing mode I, mode II, and mixed-mode tests. However, measuring interfacial properties of multi-directional laminates is not often done because of the difficulties associated with the migrations of the delamination plane. Therefore, the interfacial properties were obtained by scaling the measured properties of tape/fabric (T/F) interfaces of specimens manufactured with the same tape and fabric materials as the 3PB specimen [27]. In T/F specimens, the delamination is bound by the fabric and 0-degree unidirectional tape plies, so migration is prevented. Migrations and matrix cracks in the 3PB specimen increase the effective toughness of the interface relative to that obtained for a T/F interface. To obtain the fracture toughnesses for damage initiation, the corresponding T/F values were increased by 70% to ensure that the separation initiates at about 8 mm of applied displacement, where the first transverse

matrix cracks were observed in the experiments. The toughnesses of the bridging law were increased by 40% to match the maximum load of the 3PB test. The bridging strengths were reduced by 40% to achieve the desired nonlinearity in the response between initiation and the maximum load. This fitting procedure is approximate, and it may not perfectly represent the fracture process at other mode mixities. Nevertheless, the result provides a good approximation of the quasi-static response of the 3PB doubler specimen, as shown in Fig. 20. The interface properties obtained by fitting the predicted quasi-static response to the experimental values are reported in Table 11.

Table 10. Material properties of IM7 SGP196P/8552 fabric plies in 3PB specimen [27].

E_{11} [MPa]	$E_{22}=E_{33}$ [MPa]	G_{12} [MPa]	$G_{12}=G_{23}$ [MPa]	ν_{12}	Ply thickness [mm]
66,000.	65,800.	5100.	3400.	0.052	2.07

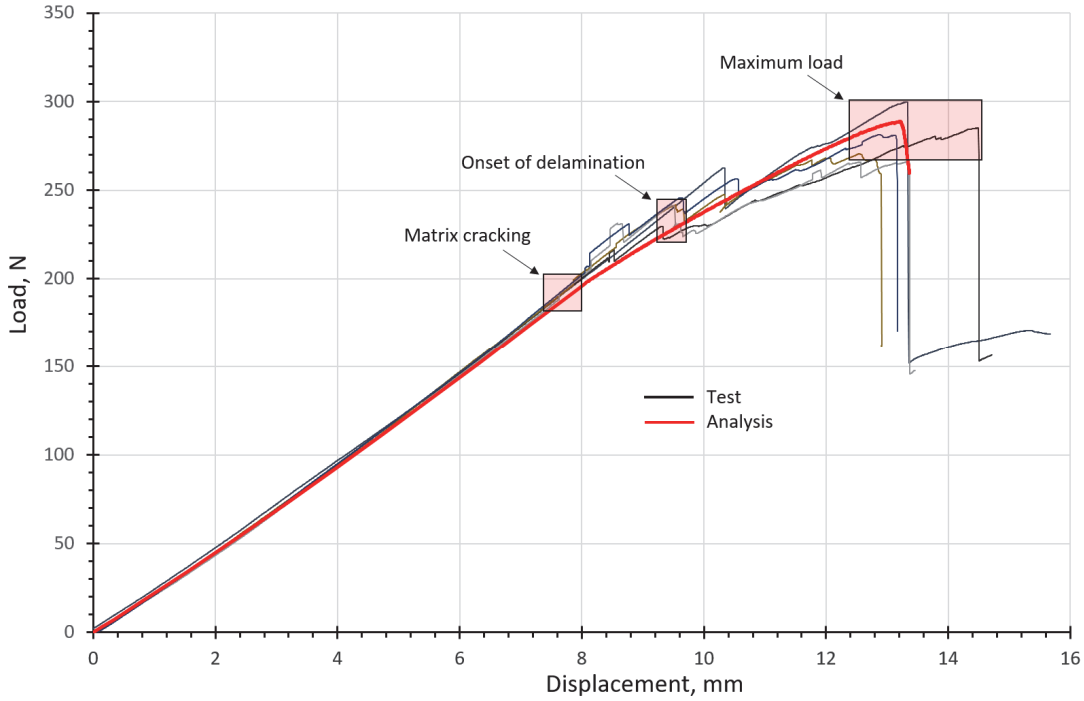

Fig. 20. Load versus displacement response of 3PB specimen.

Table 11. Effective properties of 3PB skin/doubler interface.

	G_{Ic} [N/mm]	G_{IIc} [N/mm]	σ_c [MPa]	τ_c [MPa]	η_{BK}
Initiation	0.35	1.0	80.	99.	2.07
Bridge	0.6	3.5	4.0	12.	3.0

5.3 Fatigue Tests and Analyses of 3PB Doubler Test

The experimental results of the 3PB doubler test indicate that the skin/doubler separation grows initially at approximately the same rate on both ends of the specimen. When the propagation length on both flange edges reaches 8 to 11 mm, the damage growth becomes unsymmetric. The damage grows unstably on one flange end, with little further growth at the other. The experimental results for $R = 0.1$ and for applied loads of $F^{max} = 155$ N, 167 N, and 214 N are represented by symbols in Fig. 21. The colored bands span the range between the propagation lengths on each end of the specimen. Three specimens were tested at $F^{max} = 214$ N, and one specimen at each of the other two loads.

The analyses of the 3PB test were conducted using the CF20 function with the parameters $\eta = 0.95$, $\varepsilon = 0.2$, $p = \beta$ determined in Section 4.3. The three solid lines correspond to the predicted results for the three applied loads. The correlation with experiments is satisfactory, considering the high sensitivity of the propagation rates to the applied load: the tests indicate that increasing the maximum applied force from 155 N to 214 N (38% increase) increases the rate of propagation by approximately 25 times.

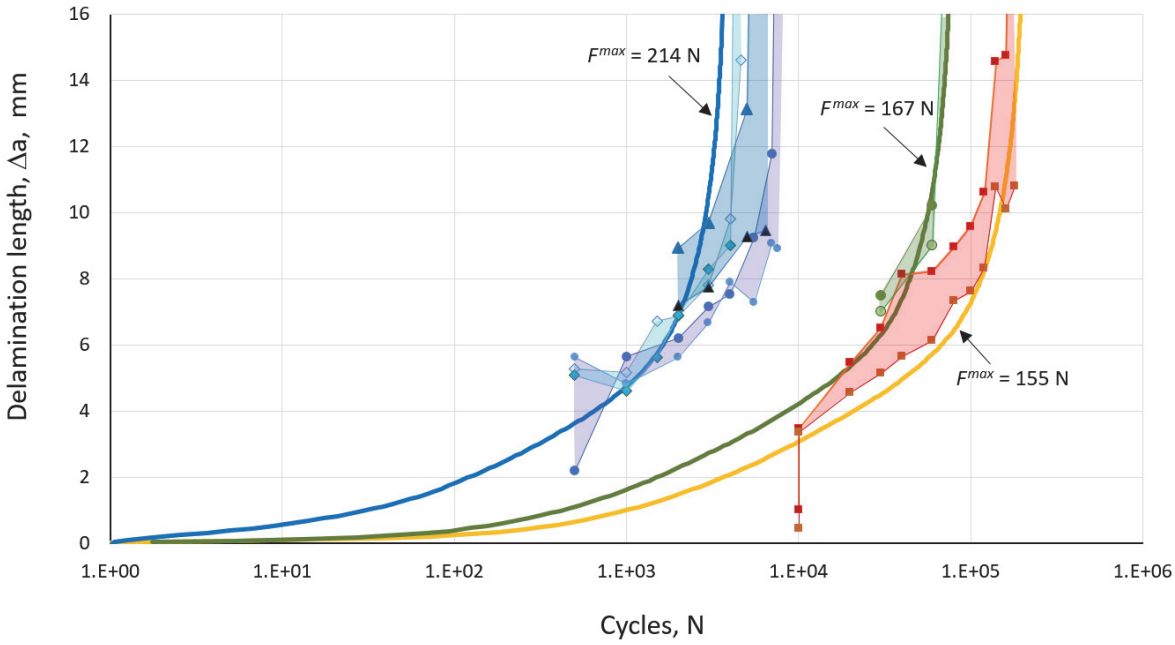

Fig. 21. Delamination length as a function of cycles for 3PB doubler test for three applied loads and with $R = 0.1$ (CF20 with $\eta = 0.95$, $\varepsilon = 0.2$, $p = \beta$).

Tests and analyses of the 3PB test were also conducted for a stress ratio $R = 0.4$ and the following maximum applied loads: $F^{max} = 178$ N, 200 N, and 214 N. The model parameters were not adjusted and remain the ones used above for $R = 0.1$. The results are shown in Fig. 22.

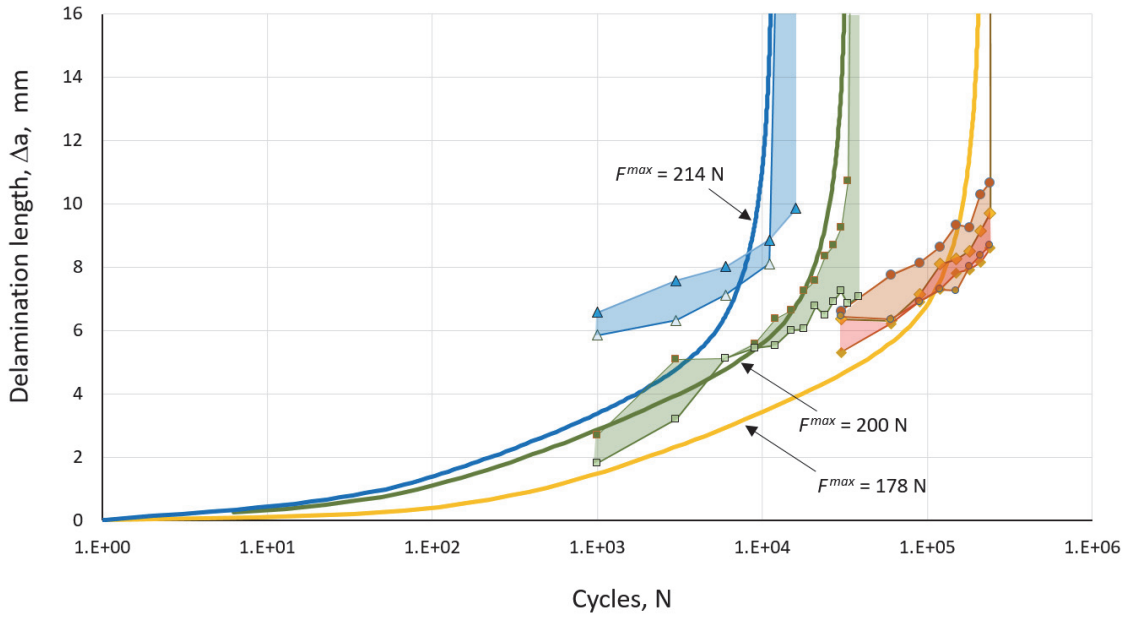

Fig. 22. Delamination length as a function of cycles for 3PB doubler test for three applied loads and with $R = 0.4$ (CF20 with $\eta = 0.95$, $\varepsilon = 0.2$, $p = \beta$).

To conclude on the analyses of the 3PB test, it is important to note that all of the test configurations and load ratios considered in this report were analyzed with the CF20 model using the same parameters ($\eta = 0.95$, $\varepsilon = 0.2$, $p = \beta$). These parameters were determined in Section 4.3 by comparing the results of the analyses of the DCB test with experimental results. In particular, it was found that the exponent of the Paris law predicted with Fleck's assumption, $\varepsilon = 1/3$, was too high and that $\varepsilon = 0.2$ produced more accurate predictions. Whether these parameters are optimal for all materials and configurations is something that still needs to be ascertained. For instance, the predictions shown in Fig. 21 overestimate somewhat the propagation rates for the highest load, and underestimate them for the lowest load. The following procedure could be used to determine the optimal value of ε.

In complex structural configurations, where the propagation rates are influenced by the initial transients and changes in the mode mixity with crack growth, the Paris law coefficients cannot be readily determined. Therefore, a means to determine ε that does not rely on standard specimens is proposed here. To illustrate the effect of ε on the results of test simulations, analyses of the 3PB specimen subjected to fatigue loading were conducted using the CF20 damage model with two applied maximum loads: $F^{max} = 214$ N and 155 N, and two values of ε, 0.2 and 1/3. The other CF20 parameters used are the ones determined in Section 4.3: $\eta = 0.95$ and $p = \beta$. The stress ratio is $R = 0.1$ for all four analyses.

Results of the simulations are shown in Fig. 23. The first observation is that, as expected, the number of cycles for a given length of propagation is much larger for $\varepsilon = 1/3$ than it is for $\varepsilon = 0.2$. More importantly, the predicted values of m can be extracted from the figure as follows. If a single Paris law is valid for the entire range of propagation, then the number of cycles to reach a crack extension Δa can be obtained by integrating the Paris law, which gives an expression of the form:

$$N(\Delta a) = F^{-2m}\,\mathrm{H} \tag{24}$$

where $N(\Delta a)$ is the number of cycles to reach a crack length a for a maximum applied load F. The term H is an unknown function of geometry, crack length, Paris law pre-factor C, and exponent m. The values of m and H can be obtained using any two points (N_i, F_i) corresponding to any delamination increment Δa. Solving for m gives:

$$m = \frac{1}{2}\frac{\log N_2 - \log N_1}{\log F_1 - \log F_2}\,. \tag{25}$$

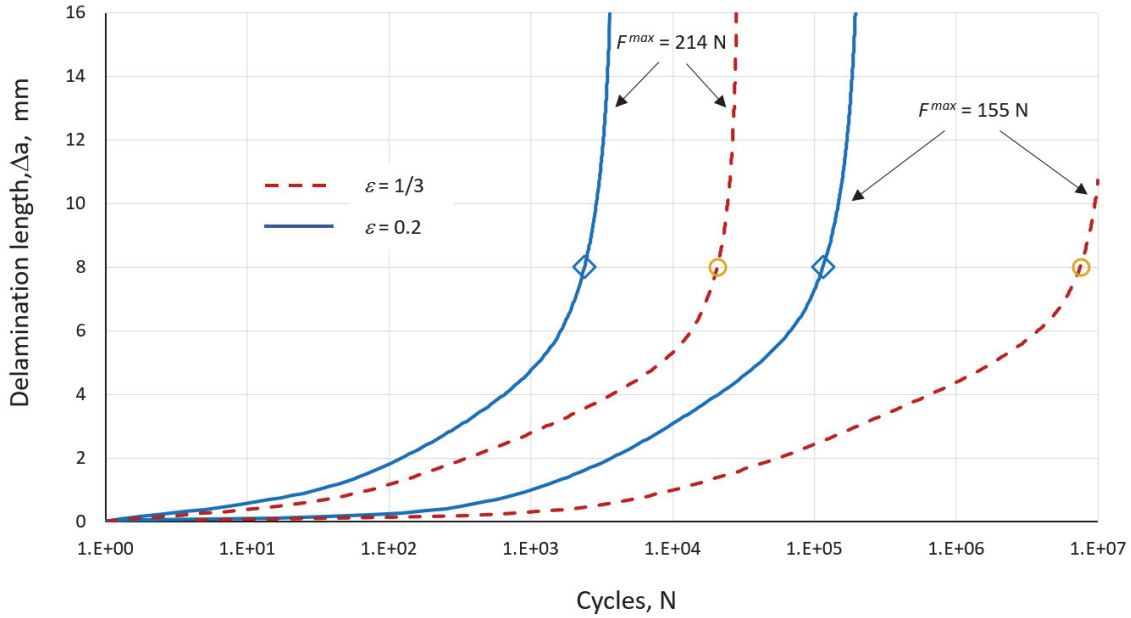

Fig. 23. Predicted delamination length as a function of cycles for 3PB specimen for two applied loads, $R = 0.1$, and using $\varepsilon = 0.2$ and 1/3 (CF20 with $\eta = 0.95$, $p = \beta$).

For example, the following sets (N_i, F_i) can be read from Fig. 23 at $\Delta a = 8$ mm: For the analyses with $\varepsilon = 0.2$, the points shown with diamond symbols are (2380, 214) and (1.16E5, 155). For $\varepsilon = 1/3$, the points shown with the open circles are (2.06E4, 214) and (7.50E6, 155). Then, Eq. 25 gives $m_{02} = 6.0$ and $m_{1/3} = 9.1$. Evaluated at $\Delta a = 4$ mm, the exponents are $m_{02} = 5.4$ and $m_{1/3} = 8.0$. Due to the R-curve response of the fracture process and the evolution of the mode mixity with crack length, m varies somewhat with crack length, but the ratio of the exponents obtained with $\varepsilon = 1/3$ and $\varepsilon = 0.2$ remains approximately constant.

Using the averages of the experimental results in Fig. 21 for $F^{max} = 155$ N and 214 N at $\Delta a = 8$ mm, gives an experimental exponent of $m_{test} \approx 5$. The corresponding value of ε can easily be estimated as follows. Allegri's [6] relationship between the exponent of the S-N curve and that of the Paris law states that $\beta_{test} = 2m_{test}$. Then, using Eqs. 4 and 19 to solve for $\varepsilon_{\text{test}}$ gives:

$$\varepsilon_{test} = \varepsilon_{analysis} \frac{1 + R - 2 \cdot 10^{\frac{7}{2m_{analysis}}}}{1 + R - 2 \cdot 10^{\frac{7}{2m_{test}}}} \ . \tag{26}$$

Substituting $R = 0.1$, $\varepsilon_{analysis} = 0.2$, $m_{analysis} = 6$, and $m_{test} = 5$ gives $\varepsilon_{test} = 0.15$. The analysis results corresponding to $\varepsilon = 0.15$ are not shown here to emphasize that a single set of parameters can provide satisfactory results for a variety of interface properties, mode mixities, stress ratios, and structural configurations.

6 Summary and Discussion

Recent advances in the understanding of fatigue initiation and propagation, including the semi-analytical models of Allegri [8] and the cohesive models developed by the first author [4], indicate that there are relationships between the material properties that describe tearing (G_c, σ_c), those that describe fatigue life (S-N), and those that describe crack propagation rates (Paris law). In the model proposed in [4], a heuristic damage accumulation law was used to relate S-N to the rate of crack propagation. That particular form of the damage function was selected because, when integrated, it provides the desired shape of an S-N diagram. However, a physical basis for the formulation of this function is still elusive. The role of the form of the damage accumulation function on the relationship between an S-N curve and its associated rate of crack propagation was evaluated in this report. Three alternative fatigue damage accumulation functions capable of reproducing equivalent S-N diagrams were developed. It was found that, for a given specimen configuration and endurance limit, all of the functions predict the same exponent m of the Paris law. With any of these functions, the experimental values of m could be predicted using a relative endurance limit at full load reversal of $\sigma_e^{max} / \sigma_c = \varepsilon = 0.2$, rather than using the value $\varepsilon = 1/3$ suggested in previous work [4, 5]. However, the analysis results also indicate that different functions predict different values of the pre-term C of the Paris law. Therefore, a fatigue damage accumulation function was selected based on simplicity, ease of use, and by comparison with experimental results.

The newly proposed function CF20 has two distinct advantages over the previous formulation. First, the parameter p offers the possibility of calibrating the model based on additional experimental results. Increasing the value of p by one approximately doubles the predicted pre-factor C of the Paris law and, consequently, also doubles the rate of propagation throughout the range of energy release rates. Experience will tell if the value of p proposed herein is universal or if it is a material property. A second advantage of importance is that the parameter β of CF20 can be calculated on the fly rather than relying on tables of pre-calculated solutions.

The effectiveness of the proposed methodology with the CF20 damage function was demonstrated by conducting analyses of a DCB test, an MMB test, and a 3PB doubler test with a unidirectional tape skin and a fabric doubler. The first two represent standard characterization tests for the interface properties of a unidirectional material. The analysis of the DCB test accounts for fiber bridging and captures accurately the lateral shifts of the Paris lines. The 3PB test analyzed presents several additional challenges. First, the 3PB doubler specimen is initially pristine, which would pose a problem for fatigue analysis methods that do not use S-N life information. Secondly,

the skin/doubler separation occurs at an interface between dissimilar tape and fabric plies, and it also involves transverse matrix cracking, delaminations, crack migrations, and bridging mechanisms. These mechanisms were represented with an effective R-curve bridging law for separation that was obtained by analysis of the quasi-static load-displacement response. Finally, the 3PB tests provide valuable data to verify the ability of the model to predict the effects of the stress factor. The results of the analyses indicate that the same set of model parameters η, ε, and p can provide accurate predictions of the rate of fatigue crack propagation for a variety of material interfaces, mode mixities, load levels, and stress ratios.

References

1. Juvinall, R. C., and Marshek, K. M., *Fundamentals of Machine Component Design*, Wiley, New York, NY, 2000.
2. Shigley, J. E., and Mitchell, L. D., *Mechanical Engineering Design*, McGraw-Hill Book Company, New York, NY, 1983.
3. Alderliesten, R. C., "Fatigue and Failure Analysis of Composite Structures Understanding the Fundamentals," TU Delft Summer School - Fatigue and Failure Analysis of Composite Structures, Delft, NL, June 2019.
4. Dávila, C. G., "From S-N to the Paris Law with a New Mixed-Mode Cohesive Fatigue Model," Technical Report NASA-TP-2018-219838, Hampton, VA, June 2018.
5. Dávila, C. G., "From S-N to the Paris Law with a New Mixed-Mode Cohesive Fatigue Model for Delamination in Composites," *Theoretical and Applied Fracture Mechanics*, Vol. 106, 2020, p. 102499.
6. Allegri, G., and Wisnom, M. R., "A Non-Linear Damage Evolution Model for Mode II Fatigue Delamination Onset and Growth," *International Journal of Fatigue*, Vol. 43, 2012, pp. 226-234.
7. Blanchfield, J. P., "Unified Nonlinear Damage Model for Fatigue Delamination Onset and Growth in Fibre Reinforced Plastics," PhD Dissertation, Department of Aerospace Engineering, University of Bristol, Bristol, UK, 2015.
8. Allegri, G., "A Unified Formulation for Fatigue Crack Onset and Growth Via Cohesive Zone Modelling," *Journal of the Mechanics and Physics of Solids*, 2020.
9. Goodman, J., *Mechanics Applied to Engineering*, Longmans, Green and Co., London, UK, 1899.
10. Fleck, N. A., Kang, K. J., and Ashby, M. F., "Overview No. 112: The Cyclic Properties of Engineering Materials," *Acta Metallurgica et Materialia*, Vol. 42, No. 2, 1994, pp. 365-381.
11. Vieira, A. P., Andrade, J. S., and Herrmann, H. J., "Subcritical Crack Growth: The Microscopic Origin of Paris' Law," *Physical Review Letters*, Vol. 100, No. 19, 2008, p. 195503.
12. Turon, A., Costa, J., Camanho, P. P., and Dávila, C. G., "Simulation of Delamination in Composites under High-Cycle Fatigue," *Composites Part A: Applied Science and Manufacturing*, Vol. 38, No. 11, 2007, pp. 2270-2282.
13. Kun, F., Carmona, H. A., Andrade, J. S., and Herrmann, H. J., "Universality Behind Basquin's Law of Fatigue," *Physical Review Letters*, Vol. 100, No. 9, 2008, p. 094301.
14. O'Brien, T. K., Chawan, A. D., Krueger, R., and Paris, I. L., "Transverse Tension Fatigue Life Characterization through Flexure Testing of Composite Materials," *International Journal of Fatigue*, Vol. 24, No. 2-4, 2002, pp. 127-145.

15. Dassault Systèmes, *Abaqus® 2017 Documentation*, Simulia Corp., Providence, RI, USA, 2017.

16. Raimondo, A., and Bisagni, C., "Analysis of Local Stress Ratio for Delamination in Composites under Fatigue Loads," *AIAA Journal*, Vol. 58, No. 1, 2020, pp. 455-463.

17. Murri, G. B., "Evaluation of Delamination Onset and Growth Characterization Methods under Mode I Fatigue Loading," NASA/TM–2013-217966, Hampton, VA, Feb. 2013.

18. Wanthal, S., Schaefer, J., Justusson, B., Hyder, I., Engelstad, S., and Rose, C. A., "Verification and Validation Process for Progressive Damage and Failure Analysis Methods in the NASA Advanced Composites Consortium," American Society for Composites 32nd Technical Conference, Purdue University, West Lafayette, IN, Oct. 2017.

19. Allegri, G., Wisnom, M. R., and Hallett, S. R., "A New Semi-Empirical Law for Variable Stress-Ratio and Mixed-Mode Fatigue Delamination Growth," *Composites Part A: Applied Science and Manufacturing*, Vol. 48, 2013, pp. 192-200.

20. Ratcliffe, J. G., and Johnston Jr, W. M., "Influence of Mixed Mode I-Mode II Loading on Fatigue Delamination Growth Characteristics of a Graphite Epoxy Tape Laminate," 29th American Society for Composites Technical Conference, La Jolla, CA, Sept. 2014.

21. ASTM_D6671/D6671M, "Standard Test Method for Mixed Mode I-Mode II Interlaminar Fracture Toughness of Unidirectional Fiber Reinforced Polymer Matrix Composites," *Annual Book of ASTM Standards*, American Society for Testing and Materials, West Conshohocken, PA, 2006.

22. Dávila, C. G., Leone Jr, F. A., Song, K., Ratcliffe, J. G., and Rose, C. A., "Material Characterization for the Analysis of Skin/Stiffener Separation," Proceedings of the American Society for Composites, West Lafayette, IN, Oct. 2017.

23. Leone Jr, F. A., Song, K., Johnston, W. M., Rose, C. A., Jackson, W. C., Kosztowny, C. J., and Dávila, C. G., "Test/Analysis Correlation of Damage States in Stiffened Post-Buckled Validation Building Block Specimens," Proceedings of the ASC 34th Technical Conference, Atlanta, GA, Sept. 2019.

24. Iarve, E. V., Hoos, K., Braginsky, M., Zhou, E., and Mollenhauer, D. H., "Progressive Failure Simulation in Laminated Composites under Fatigue Loading by Using Discrete Damage Modeling," *Journal of Composite Materials*, Vol. 51, No. 15, 2017, pp. 2143-2161.

25. Selvarathinam, A. S., Perera, S., Smith, G., Schaefer, J., Johnston, W. M., Jackson, W. C., Rose, C. A., and O'Brien, T. K., "Evaluation of BSAM (B-Spline Analysis Method) for Residual Strength and Life Prediction Using Three-Point Bend Doubler under Quasi-Static and Cyclic Loading," Proceedings of the AIAA Scitech 2020 Conference, Jan. 2020, pp. 1476.

26. Selvarathinam, A. S., De Carvalho, N. V., Seshadri, B. R., and Johnson, V., "Validation of Floating Node Method Using Three-Point Bend Doubler under Quasi-Static Loading," Proceedings of the AIAA Scitech 2019 Conference, San Diego, CA, 7-11 Jan. 2019, pp. 1549.

27. Dávila, C. G., and Ratcliffe, J. G., "Quasi-Static and Fatigue Delamination at Tape/Fabric Interfaces," Proceedings of the AIAA SciTech Conference, Orlando, FL, Jan. 2020, pp. 1384.

REPORT DOCUMENTATION PAGE

Form Approved
OMB No. 0704-0188

1. REPORT DATE *(DD-MM-YYYY)*	2. REPORT TYPE	3. DATES COVERED *(From - To)*
01-04- 2020	Technical Publication	

4. TITLE AND SUBTITLE

Evaluation of Fatigue Damage Accumulation Functions for Delamination Initiation and Propagation

5a. CONTRACT NUMBER

5b. GRANT NUMBER

5c. PROGRAM ELEMENT NUMBER

6. AUTHOR(S)

Carlos G. Dávila; Cheryl A. Rose; Gretchen B. Murri;Wade C. Jackson; William M. Johnston

5d. PROJECT NUMBER

5e. TASK NUMBER

5f. WORK UNIT NUMBER

081876.02.07.18.01.03.02

7. PERFORMING ORGANIZATION NAME(S) AND ADDRESS(ES)

NASA Langley Research Center
Hampton, VA 23681-2199

8. PERFORMING ORGANIZATION REPORT NUMBER

L-21138

9. SPONSORING/MONITORING AGENCY NAME(S) AND ADDRESS(ES)

National Aeronautics and Space Administration
Washington, DC 20546-0001

10. SPONSOR/MONITOR'S ACRONYM(S)

NASA

11. SPONSOR/MONITOR'S REPORT NUMBER(S)

NASA/TP-2020-220584

12. DISTRIBUTION/AVAILABILITY STATEMENT

Unclassified - Unlimited
Subject Category 24
Availability: STI Program (757) 864-9658

13. SUPPLEMENTARY NOTES

14. ABSTRACT

A new damage accumulation function that provides a link between the S-N diagram that describes crack initiation, and the Paris law that characterizes the rate of crack propagation was developed. This function is particularly useful for analysis because of the ease with which the model parameters can be determined with a minimal amount of experimental information. The effectiveness of the proposed methodology was demonstrated by conducting analyses of a double cantilever beam test, a mixed-mode bending test, and a three-point bending test of a skin/doubler specimen subjected to several loading conditions. The results indicate that the same set of model parameters can provide accurate predictions of the rate of fatigue crack propagation for a variety of material interfaces, mode mixities, load levels, and stress ratios.

15. SUBJECT TERMS

cohesive elements; crack propagation rate; delamination; dkin/stiffener debonding; fatigue

16. SECURITY CLASSIFICATION OF:			17. LIMITATION OF ABSTRACT	18. NUMBER OF PAGES	19a. NAME OF RESPONSIBLE PERSON
a. REPORT	b. ABSTRACT	c. THIS PAGE			STI Help Desk (email: help@sti.nasa.gov)
					19b. TELEPHONE NUMBER *(Include area code)*
U	U	U	UU	38	(757) 864-9658